5-1-2009

Structure-property stress state dependent relationships under varying strain rates

Matthew Taylor Tucker

STRUCTURE-PROPERTY STRESS STATE DEPENDENT RELATIONSHIPS

UNDER VARYING STRAIN RATES

By

Matthew Taylor Tucker

A Dissertation
Submitted to the Faculty of
Mississippi State University
in Partial Fulfillment of the Requirements
for the Degree of Doctor of Philosophy
in Mechanical Engineering
in the Department of Mechanical Engineering

Mississippi State, Mississippi

May 2009

STRUCTURE-PROPERTY STRESS STATE DEPENDENT RELATIONSHIPS

UNDER VARYING STRAIN RATES

By

Matthew Taylor Tucker

Approved:

Mark F. Horstemeyer Center for Advanced Vehicular Systems Chair in Computational Solid Mechanics Professor of Mechanical Engineering (Major Professor)	Douglas J. Bammann Professor of Mechanical Engineering (Committee Member)
John T. Berry Professor of Mechanical Engineering (Committee Member)	Phillip M. Gullett Assistant Professor of Civil Engineering (Committee Member)
Haitham El Kadiri Assistant Research Professor Center for Advanced Vehicular Systems	Sarah A. Rajala Dean of the Bagley College of Engineering

Steven R. Daniewicz
Professor of Mechanical Engineering
(Graduate Coordinator)

Name: Matthew Taylor Tucker

Date of Degree: May 02, 2009

Institution: Mississippi State University

Major Field: Mechanical Engineering

Major Professor: Dr. Mark F. Horstemeyer

Title of Study: STRUCTURE - PROPERTY STRESS STATE DEPENDENT RELATIONSHIPS UNDER VARYING STRAIN RATES

Pages in study: 91

Candidate for degree of Doctor of Philosophy

In this work, the microstructural effects of stress state and strain rate dependent plasticity, damage, and failure of aluminum and magnesium alloys were examined. Several experimental techniques were employed to implement the test data into a physics-based internal state variable plasticity-damage model. Effects arising from various strain rates, stress states, and material orientations were quantified and discussed within the framework of linking microstructural features to mechanical properties. The method developed for determining structure-property relations was validated by accurately capturing the effects for a variety of materials and loading conditions. The end result is a methodology capable of predicting the onset of damage and failure for a material loaded under complex dynamic conditions.

DEDICATION

I would like to dedicate this work to my incredible wife Laura who I appreciate more than I could ever express. You have supported me unconditionally and I will never be able to adequately repay you. I vow to daily do my best though.

ACKNOWLEDGMENTS

First, I would be remiss without acknowledging my wife who especially deserves praise for always being there for me. She is the epitome of love and support and it has helped me greatly. My parents instilled in me the importance of work and education in me as a child and also for their unquestionable support which have tremendous helps

The immense amount of help through this entire process my advisor, Dr. Mark Horstemeyer, has provided must be acknowledged. He has given guidance and encouragement from day one. I truly appreciate Dr. John Berry igniting an interest for materials science in me as an undergraduate and continuing to nurture it throughout my studies. Dr. Doug Bammann, through numerous conversations and two of the best courses I have ever taken allowed me a glimpse into the fascinating and sometimes frustrating world of material modeling. Dr. Gerard Gary has unquestionably been my experimentation mentor. The Atlantic has truly never been an obstacle in getting his honest advice and I am sure he has helped me more than he realizes. Dr. Haitham el Kadiri has helped me wade through the world of magnesium and continues to provide valuable insight whenever I ask. Dr. Phil Gullett gave me the freedom to pursue the areas of the research that I found interesting and it made the work more fun. Dr. Kiran Solanki has always been there to help me with whatever I needed, whenever I needed it. Wilburn Whittington has been a tremendous help with experiments and microstructural analysis. This work would not have been possible without countless hours for Wil in the lab.

Stephen Horstemeyer has provided machining, fabrication, and design assistance and it is all greatly appreciate. All the rest of the guys who have been here with me including Brian, Neil, Jesse, Justin, Paul, Claudio, Raj, Wes, Andy, and others have been great encouragers through the process. I only hope I returned the favor.

I consider everyone mentioned above a dear friend and that has turned out to be the most important thing by far. The friendships I have made during this process are what I will cherish the most.

I also want to thank TARDEC/DOD and the Bagley College of Engineering for their financial support. Finally, I want to thank my Lord and Savior for His steadfast goodness and grace.

TABLE OF CONTENTS

LIST OF TABLES

TABLE

LIST OF FIGURES

FIGURE

CHAPTER I

INTRODUCTION

The plasticity, damage, and failure of a ductile material are highly dependent on the structure of the material and the manner in which it is loaded. Understanding the effects of the various factors associated with ductile failure is critical for predicting the behavior of a component under varying loading scenarios. The effect of dynamic loading is becoming increasingly important to understand as the need for lighter and more efficient, yet safe vehicles continues to grow. Linking the microstructural and mechanical properties requires both accurate experimentation and physics-based internal state variable modeling. The necessary experimentation consists of acquiring stress-strain data under differing stress states and strain rates as well as microstructural analysis needed to characterize the effect of loading the on the evolution of the structure so that structure-property relationships can be established. The internal state variable modeling consists of capturing the history effects of the material and the ability to predict the effects on the microstructure of various loading scenarios. The purpose of this work is the generation of a new paradigm for evaluating high rate phenomena by introducing the quantification of damage evolution of various materials with differing microstructural alloys. By employing testing and validation at varying strain rates and stress states, the robustness of the methodology will be verified.

Chapter II presents a brief introduction to the modeling methodology implemented in the remainder of the work. The links between microstructural properties and mechanical properties are established. An explanation of the internal state variables used in the subsequent modeling is given.

Chapter III presents experimental results related to the effects of loading orientation on a wrought magnesium alloy. AZ31B was tested in compression in the rolling, transverse, and normal directions under quasi-static and high strain rate conditions. The resulting mechanical response was found to be highly dependent on the loading orientation and the role of twinning and dislocation slip is discussed as an explanation. Pertinent microstructural properties were quantified for future implementation into a material model.

Chapter IV presents the results of a comprehensive study of the stress state and strain rate effects on the plasticity, damage evolution, and fracture of three aluminum alloys produces by three different forming methods. Each material was systematically tested under tension, torsion, and compression at quasi-static and high strain rates and the damage nucleation site evolution was tracked for each scenario providing a complete characterization of the stress state and strain rate effects for each material. The test data was then used to determine the modeling constants for implementation in the internal state variable

Chapter V presents experimental and three-dimensional dynamic modeling results of a comparison of different methods currently in use to obtain high strain rate tensile and torsion/shear data. Aluminum alloy 6061 was used for the study and excellent agreement

between the experimental data and simulation results were obtained. The effect of the stress state on the fracture of the alloy was also investigated.

Lastly, Chapter VI summarizes the results of the work performed in this research and also presents recommendations for future research.

CHAPTER II

MICROSTRUCTURE - MECHANICAL PROPERTY MODEL

Microstructural features and loading history often have a profound effect on the performance and failure of structural components. The material being used, the forming processes, environment in which it is used, and loading conditions can greatly affect the relevance of the features such as voids, cracks, and particles. Traditionally simple failure criteria such as von Mises or Tresca equivalent stress have been used to design components, but safe and efficient designs are not always achieved. Without including the effect of microstructural properties and loading histories, inadequate and wasteful designs can result.

Internal state variable (ISV) evolution equations formulated at the macroscale level are an effective way to capture the structure-property relations and history effects of a material. Using ISVs to represent smaller scale microstructural constituents allows for the inclusion of history effects in the material model. This allows for the linking of relevant mechanical properties such as stress and strain to be coupled with key microstructural and processing parameters such as particle size, orientation, and spacing; interfacial strength and toughness; and texture.

The microstructure-property relationship modeling framework used here accounts for stress-state-dependent damage evolution. The constitutive model of (Bammann et al.,

1984, 1989, 1990, 1993, 1995, 1996) contains internal state variables to account for the motion of dislocations and the evolution of dislocation structures. These variables are a critical part of the constitutive analysis and are discussed in this chapter. The equations developed and used for this work were developed at the macroscale level for a cast aluminum alloy and might require slight modification for different materials depending on the pertinent deformation mechanisms. The pertinent equations in this model are denoted by the rate of change of the observable and internal state variables. The rate equations are presented in this chapter and the relationship to multiscale modeling is briefly discussed. For more details about the equations, the reader can refer to Horstemeyer et al. (1999; 2000; 2003). The equations used within the context of the finite element method are the rate of change of the observable and internal state variables given by

$$\overset{\circ}{\underline{\sigma}} = \lambda(1-\phi)tr\left(\underline{D}^e\right)\underline{I} + 2\mu(1-\phi)\underline{D}^e - \left(\frac{\dot{\phi}}{1-\phi}\right)\underline{\sigma} \tag{2.1}$$

where $\underline{\sigma}$ and $\overset{\circ}{\underline{\sigma}}$ are the Cauchy stress and the co-rotational rate of the Cauchy stress, respectively; ϕ is an ISV that represents the damage state with $\dot{\phi}$ representing its material time derivative; λ and μ are the elastic Lame constants; $\underline{D}^e$ is the elastic deformation tensor; and $\underline{I}$ is the second-order identity tensor. The underscore symbol indicates a second rank tensor. The plastic deformation tensor or inelastic flow rule, $\underline{D}^p$, is given by the relationship

$$\underline{D}^p = f(T)\sinh\left\{\frac{\left\|\underline{\sigma}'-\underline{\alpha}\right\| - \left[R+Y(T)\right](1-\phi)}{V(T)(1-\phi)}\right\}\frac{\underline{\sigma}'-\underline{\alpha}}{\left\|\underline{\sigma}'-\underline{\alpha}\right\|} \tag{2.2}$$

where $\underline{\sigma}'$ is the deviatoric part of stress tensor; T is temperature in Kelvin; $\underline{\alpha}$ is the kinematic hardening (an ISV reflecting the effect of anisotropic dislocation density); and R is the isotropic hardening (an ISV reflecting the effect of global dislocation density). The function $V(T)$ determines the magnitude of rate-dependence on yielding; $f(T)$ determines when the rate-dependence affects initial yielding; and $Y(T)$ is the rate-independent yield stress. Functions $V(T)$, $Y(T)$, and $f(T)$ are related to yielding with Arrhenius-type temperature dependence and are given as

$$V(T) = C_1 e^{\left(-C_2/T\right)} \tag{2.3a}$$

$$Y(T) = C_3 e^{\left(-C_4/T\right)} \tag{2.3b}$$

$$f(T) = C_5 e^{\left(-C_6/T\right)} \tag{2.3c}$$

where C_1 through C_6 are the yield stress related material parameters that are obtained from isothermal compression tests with variations in temperature and strain rate.

The co-rotational rate of the kinematic hardening, $\overset{o}{\underline{\alpha}}$ and the material time derivative of isotropic hardening, $\dot{R}$ are expressed in a hardening-recovery format as

$$\overset{o}{\underline{\alpha}} = \left\{ h(T)\underline{D}^p - \left[\sqrt{\frac{2}{3}} r_d(T) \left\| \underline{D}^p \right\| + r_s(T) \right] \|\underline{\alpha}\| \underline{\alpha} \right\} \left[\frac{DCS_0}{DCS} \right]^z \tag{2.4}$$

$$\dot{R} = \left\{ H(T)\underline{D}^p - \left[\sqrt{\frac{2}{3}} R_d(T) \left\| \underline{D}^p \right\| + R_s(T) \right] R^2 \right\} \left[\frac{DCS_0}{DCS} \right]^z \tag{2.5}$$

where DCS_0, DCS, and z parameters capture the microstructure effect of grain size. The dislocation populations and morphology within crystallographic materials exhibit two types of recovery. In Eqs. (2.4) and (2.5), $r_d(T)$ and $R_d(T)$ are scalar functions of temperature that describe dynamic recovery, $r_s(T)$ and $R_s(T)$ are scalar functions that describe thermal (static) recovery, whereas $h(T)$ and $H(T)$ represent anisotropic and isotropic hardening modulus, respectively. These functions are calculated as

$$r_d(T) = C_7\left[1 + C_a\left(\frac{4}{27} - \frac{J_3'^2}{J_2'^3}\right) - C_b\left(\frac{J_3'}{J_2'}\right)^{3/2}\right]e^{\left(-C_8/T\right)} \tag{2.6a}$$

$$R_d(T) = C_{13}\left[1 + C_a\left(\frac{4}{27} - \frac{J_3'^2}{J_2'^3}\right) - C_b\left(\frac{J_3'}{J_2'}\right)^{3/2}\right]e^{\left(-C_{14}/T\right)} \tag{2.6b}$$

$$r_s(T) = C_{11}e^{\left(-C_{12}/T\right)} \tag{2.6c}$$

$$R_s(T) = C_{17}e^{\left(-C_{18}/T\right)} \tag{2.6d}$$

$$h(T) = C_9\left[1 + C_a\left(\frac{4}{27} - \frac{J_3'^2}{J_2'^3}\right) + C_b\left(\frac{J_3'}{J_2'}\right)^{3/2}\right]e^{\left(-C_8/T\right)} - C_{10}T \tag{2.6e}$$

$$H(T) = C_{15}\left[1 + C_{22}\left(\frac{4}{27} - \frac{J_3'^2}{J_2'^3}\right) + C_b\left(\frac{J_3'}{J_2'}\right)^{3/2}\right]e^{\left(-C_8/T\right)} - C_{16}T \tag{2.6f}$$

where $J_2' = \frac{1}{2}\left(\underline{\sigma}' - \underline{\alpha}\right)^2$, $J_3' = \frac{1}{3}\left(\underline{\sigma}' - \underline{\alpha}\right)^3$, C_7 through C_{12} are the material plasticity parameters related to kinematic hardening and recovery terms, C_{13} through C_{18} are the

material plasticity parameters related to isotropic hardening and recovery terms, whereas C_a and C_b are the material plasticity parameters related to dynamic recovery and anisotropic hardening terms, respectively. Constants C_1 through C_{18} are determined from macroscale experiments at different temperatures and strain rates.

The damage variable, $\dot{\phi}$ represents the damage fraction of material within a continuum element. The mechanical properties of a material depend upon the amount and type of micro-defects within its structure. Damage growth is determined by the accumulation of these micro-defects. The two components of damage progression mechanism are void nucleation and growth from second phase particles and pores. In this regard, the material time derivative of damage, $\dot{\phi}$ is expressed as

$$\dot{\phi} = \left(\dot{\phi}_{particles} + \dot{\phi}_{pores}\right)c + \left(\phi_{particles} + \phi_{pores}\right)\dot{c} \tag{2.7}$$

where $\phi_{particles}$ represents void growth from particle debonding and fracture; ϕ_{pores} represents void growth from pores; with $\dot{\phi}_{particles}$ and $\dot{\phi}_{pores}$ representing their respective time derivatives; parameter c represents the void coalescence, or void interaction, that is indicative of pore-pore and particle-pore interactions with $\dot{c}$ as its time derivative. The particle- and pore-based void growth rate and the void-coalescence rate equations are given as

$$\dot{\phi}_{particles} = \dot{\eta}v + \eta\dot{v} \tag{2.8a}$$

$$\dot{\phi}_{pores} = \left[\frac{1}{\left(1-\phi_{pores}\right)^{m}} - \left(1-\phi_{pores}\right)\right]\sinh\left[\frac{2\left(2^{V(T)/Y(T)}-1\right)}{\left(2^{V(T)/Y(T)}+1\right)}\frac{\sigma_H}{\sigma_{vm}}\right]\left\|\underline{D}^{p}\right\| \tag{2.8b}$$

$$\dot{c} = \left[Cd_1 + Cd_2\left(\eta\dot{v} + \dot{\eta}v\right)\right]e^{(C_{CT}T)}\left(DCS_0/DCS\right)^{z} \tag{2.8c}$$

where v is the void growth; η is the void nucleation, whereas σ_H and σ_{vm} are the hydrostatic and von Mises stresses, respectively. The parameters Cd_1 and Cd_2 are related to first and second normalized nearest neighbor distance parameters, respectively, and C_{CT} is the void-coalescence temperature dependent parameter. The void nucleation rate and void growth rate are given as

$$\dot{\eta} = \left\|\underline{D}^{p}\right\|\frac{C_{coeff}d^{1/2}}{K_{IC}f^{1/3}}\eta\left[a\left(\frac{4}{27}-\frac{J_3^{\,2}}{J_2^{\,3}}\right)+b\frac{J_3}{J_2^{3/2}}+c\left\|\frac{I_1}{\sqrt{J_2}}\right\|\right]e^{\left(-C_{\eta T}/T\right)} \tag{2.9a}$$

$$\dot{v} = \frac{\sqrt{3}R_0}{2(1-m)}\left[\sinh\left(\sqrt{3}(1-m)\frac{\sqrt{2}I_1}{3\sqrt{J_2}}\right)\right]\left\|\underline{D}^{P}\right\| \tag{2.9b}$$

where C_{coeff} is a material constant that scales the response as a function of initial conditions; d is the particle size; K_{IC} is the fracture toughness; f is the volume fraction of second-phase particles; $C_{\square T}$ is the void nucleation temperature dependent parameter; I_1, J_2, and J_3 are the independent stress invariants; m void growth constant; R_0 is the initial void radius, whereas material constants a, b, and c are the void-nucleation constants that are determined from different stress states (i.e., a is found from a torsion test, while b and

c are determined from tension and compression tests, with all three having units of stress).

The time integral form of Equation (2.7) is used as the damage state. Based on this ISV model, material failure is assumed to occur when Equation (2.7) reaches unity ($\phi \to 1.0$) within a finite element. For all practical purposes, material failure can be assumed at a much smaller value (safe limit) of ϕ as the damage increases very rapidly to 1.0 shortly after ϕ reaches a small percentage. By including damage, ϕ as an ISV, different forms of damage rules can be incorporated easily into the constitutive framework. In summary, α, R, σ, c, v, and η in Equations. (2.1) through (2.9) represent the ISVs in this microstructure-property relationship material model.

REFERENCES

Bammann, D. J. (1984) 'An internal variable model of viscoplasticity', *International Journal Engineering Science*, Vol. 8-10, pp. 1041-1053.

Bammann, D.J. and Aifantis, E.C. (1989) 'A damage model for ductile metals', *Nuclear Engineering and Design*, Vol. 116, pp. 355-362.

Bammann, D.J. (1990) 'Modeling temperature and strain rate dependent large deformations of metals', *Applied Mech. Rev*., Vol. 1, pp. 312-318.

Bammann, D. J., Chiesa, M. L., Horstemeyer, M. F., and Weingarten, L. I. (1993), 'Failure in ductile materials using finite element methods', Structural Crashworthiness and Failure, edited by T. Wierzbicki and N. Jones, Elsevier Applied Science, The Universities Press (Belfast) Ltd.

Bamman, D. J., Chiesa, M. L., and Johnson, G. C. (1995) 'A state variable damage model for temperature and strain rate dependent metals, Constitutive laws: theory, experiments, and numerical implementation', eds. A. M. Rajendran and R. C. Batra, CIMNE, Barcelona, pp. 84-97.

Bammann, D.J., Chiesa, M.L., Johnson, G.C. (1996), 'Modeling large deformation and failure in manufacturing processes', *Theoretical and Applied Mechanics*, eds. T. Tatsumi, E. Wannabe, and T. Kambe, Elsevier Science, pp. 359-376.

Horstemeyer, M.F. and Gokhale, A.M. (1999) 'A void-crack nucleation model for ductile metals', *International Journal of Solids and Structures*, Vol. 36, pp. 5029-5055.

Horstemeyer, M.F, Lathrop, J., Gokhale, A.M., Dighe, M. (2000) 'Modeling stress state dependent damage evolution in a cast Al-Si-Mg aluminum alloy' *Theoretical and Applied Fracture Mechanics*, Vol. 33, pp. 31-47.

Horstemeyer, M.F., Wang, P. (2003) 'Cradle-to-grave simulation-based design incorporating multiscale microstructure-property modeling: reinvigorating design with science', *Journal of Computer-Aided Materials Design*, Vol. 10, pp. 13-34, 2003.

CHAPTER III

ANISOTROPIC EFFECTS ON THE STRAIN RATE DEPENDENCE OF A WROUGHT MAGNESIUM ALLOY

INTRODUCTION

The need for understanding the plastic deformation behavior of lightweight alloys is of great interest to various industries. In particular, the high strain rate response of these materials is of great importance to the automotive, aerospace, and defense related industries especially as the need for lighter yet stronger vehicles continues to increase. Because of their high strength-to-weight ratios, magnesium alloys in particular have the potential to replace steel or aluminum components currently in use. AZ31B, also referred to as Mg-3Al-1Zn, is a wrought alloy and has been proposed as a replacement for structural steel and aluminum alloys.

Some work has been performed in providing understanding of the microstructural characteristics and mechanical properties of magnesium alloys. However, the effect of strain rate and the accompanying structure-property relationships for these materials have not been comprehensively investigated. Since the applications in which components will be subjected include impact loads, whether they are an automobile crash or a projectile impact, understanding the behavior of the material to high strain rate loading is

paramount. This study serves as a first step toward modeling the high rate structure-property relations of AZ31B.

The previous work performed on magnesium and its alloys has largely focused on the deformation mechanisms and the temperature and texture effects on the mechanical response to quasi-static loading. For instance, the effect of the grain size on the deformation characteristics was investigated, and it was found that the grain size affected the shape of the characteristic "concave" flow stress curve, resulting from the effect of twinning on slip, as well as the Hall-Petch slope (Barnett et al. 2004). The effect of temperature has been observed for AZ31B such that the strain rate sensitivity increased with an increased temperature as well as the onset of dynamic recrystallization at approximately 200ºC (Agnew and Duygulu 2005). The role of texture on the mechanical properties is also important as the flow stress and tensile elongation are highly dependent on the loading conditions and crystal orientation (Kim and Kim 2004). Jain and Agnew (2007) found that the yield strength in the rolling direction was insensitive to temperature and linked the insensitivity to twinning.

Other work has focused on the effect of low and high strain rates on the flow stress and the associated deformation mechanisms in cast and homogenized AZ31B (Ishikawa et al. 2005a) where it was found that at strain rates below 10^{-1} /s, dislocation creep by pipe diffusion was dominant at low temperatures while lattice diffusion dominated high temperature deformation. At strain rates above 10^{3} /s, dislocation glide and twinning dominated the response. Hence, the compiled work of Barnett (Barnett et al. 2004), Agnew and Duygulu (2005), Kim and Kim (2004), and Ishikawa et al. (2005a) provide a basis for understanding the effects of temperature, grain size, and texture on the

mechanical response of AZ31B. Ishikawa et al (2005b) also studied the effect of temperature and strain rate on magnesium alloy AZ91 and found that even at elevated temperatures, high strain rate deformation proceeded by dislocation glide and twinning. The effect of texture on the high strain rate response has not yet been fully quantified.

Mukai et al performed studies in which a refined grain structure for magnesium alloys AZ31, ZK60 (Mukai et al. 2003) and pure magnesium (Mukai et al. 2001) enhanced the tensile strength and ductility under dynamic loads. Modifying the texture through equal-channel-angular-extrusion was found to further enhance the ductility of alloys AZ31 and ZK60 (Mukai et al. 2003). Livescu et al (2006) studied the mechanical response and texture evolution during the high strain rate deformation of pure magnesium and alloy AZ31 and found that the stress-strain response in the rolling and transverse directions were strain rate insensitive while the response in the normal direction was highly strain rate dependent.

EXPERIMENTAL PROCEDURES

To fully quantify the effect of the loading orientation and strain rate on the stress-strain behavior of AZ31B, compression tests at quasi-static and high strain rates were performed in all three directions as indicated by Figure 3.1. All of the specimens were tested to fracture. The specimens were obtained from an as-received 19.05 mm thick plate in the H24 condition. Tests under quasi-static conditions were performed using an Instron 5882 electromechanical machine under constant strain rate controlled at 10^{-3}/s. The high strain rate tests were conducted using a maraging steel Split Hopkinson

Pressure Bar (SHPB) apparatus. The analysis of the high strain rate data was conducted using the DAVID software package (Gary 2005).

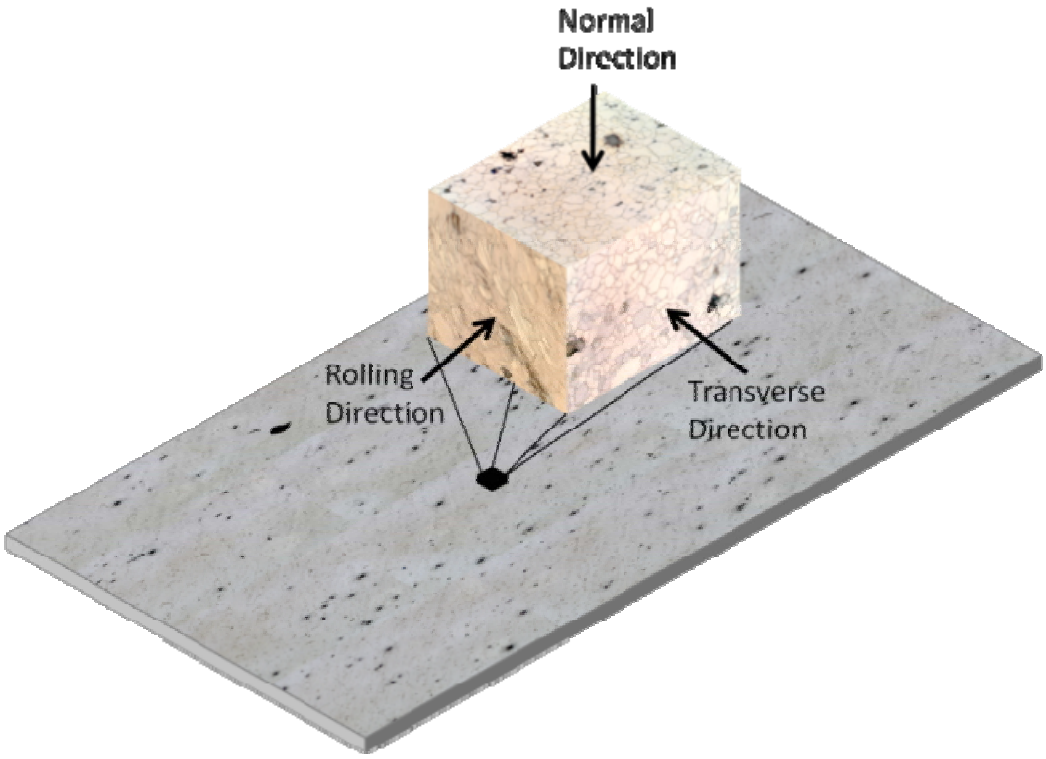

Figure 3.1. Orientations of testing and miocrostructural analysis relative to the as-received AZ31B plate.

EXPERIMENTAL RESULTS

Figure 3.2 shows the results of tests performed at quasi-static (10^{-3}/s) and high strain rates (3400/s – 4300/s). The test results corresponded well to tests conducted by Livescu et al (2006).

When tested in the normal or short transverse direction, a strong rate dependence on the yield strength was evident. The initial hardening rate at high strain rate was similar to that at quasi-static rates, but the high strain rate specimen began to exhibit softening at a strain of approximately 0.08 which continued until the specimen fractured at a strain of approximately 0.18.

This constituted a significant increase in the strain-to-failure compared to the quasi-static conditions and is likely due to thermal softening during the adiabatic conditions of the high rate test. The effect of specimen geometry was studied as for inertial effects by testing larger specimens both in length and diameter at the same strain rates. The same increased strain to failure was observed eliminating the effect of inertia. The onset of dynamic recrystallization was also considered as a source for the increased strain-to-failure, but the metallographic analysis did not reveal any supporting evidence.

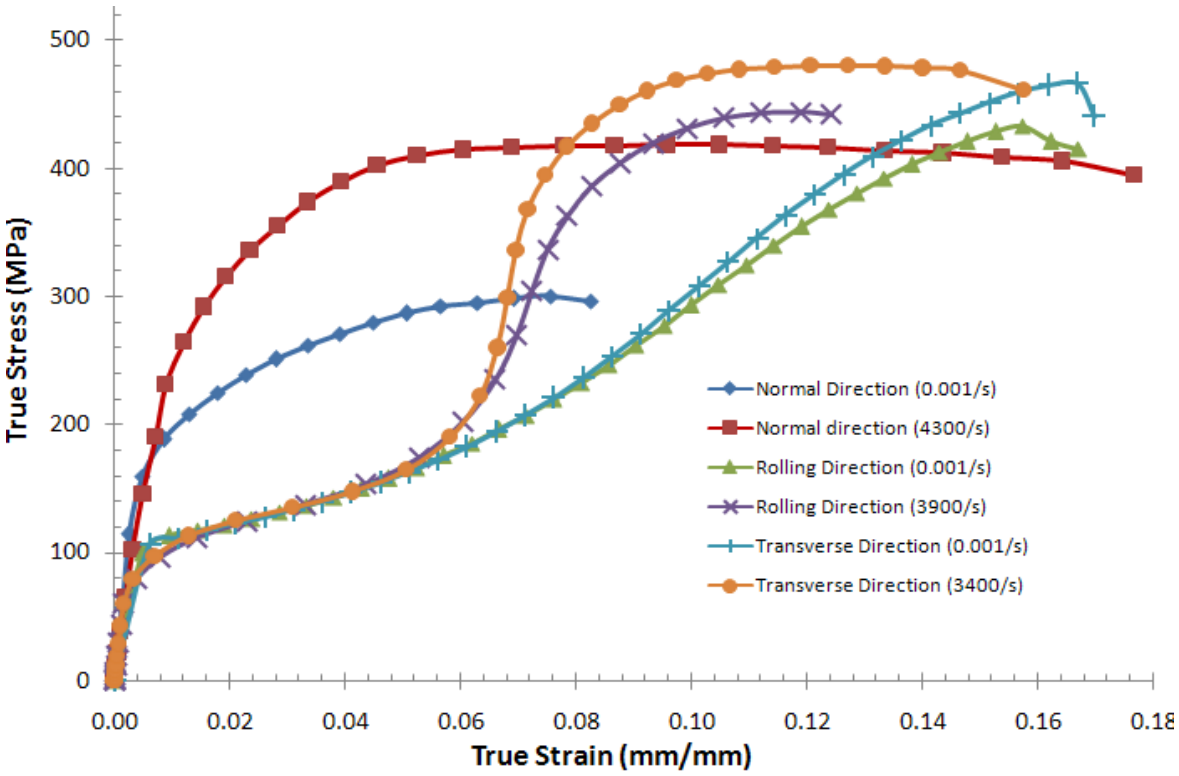

Figure 3.2. Compressive stress–strain behavior of AZ31B-H24 showing the anisotropic effects on the strain rate dependence.

To verify this increased strain-to-failure, statistical analyses of quasi-static and high strain rate tests were performed. The mean strain-to-failure for six quasi-static tests was 0.079 with a standard deviation of 0.0004. The mean strain-to-failure of seven high rate tests was 0.16 with a standard deviation of 0.06. The results of two of the high rate tests were further verified using a high speed camera to optically determine the strain at fracture initiation. The fracture strain evident from the high speed images corresponded to the failure initiation evident from the high rate data. Figure 3.3 shows six frames from a compression test of AZ31B in the normal direction conducted at approximately 4000/s. A crack indicating initial failure is evident in the fourth image. The third image indicates a strain of approximately 0.2 at which point no crack is evident.

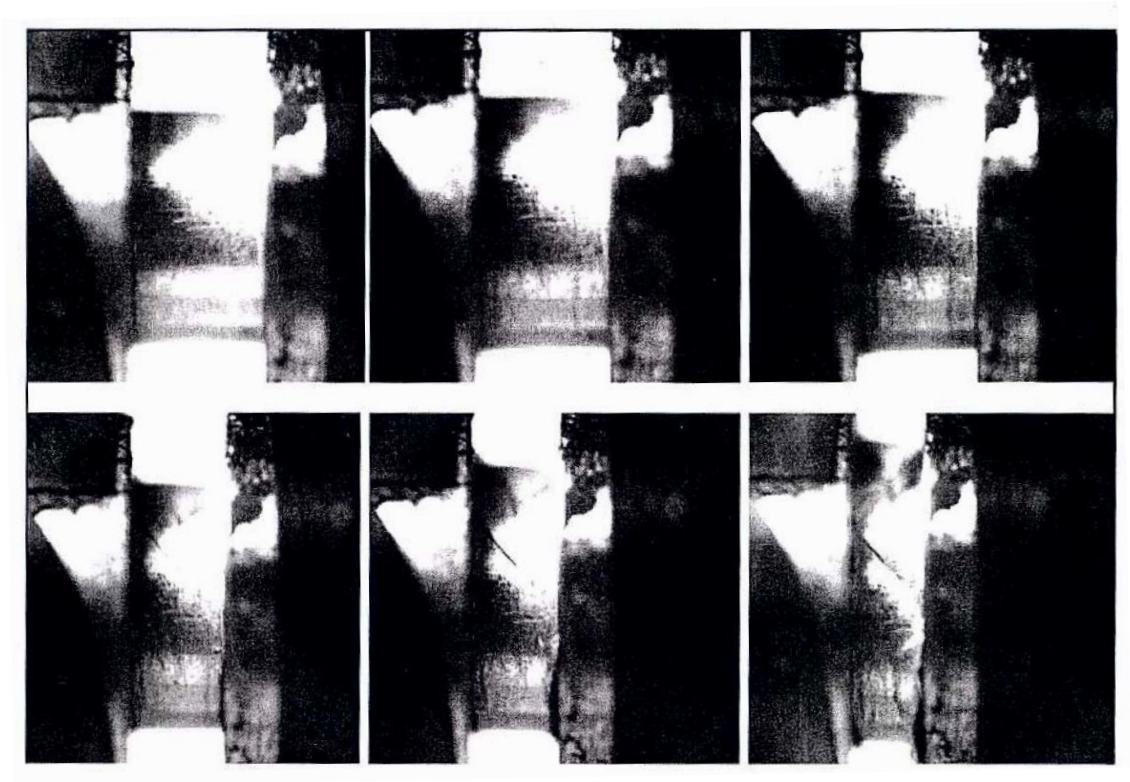

Figure 3.3. High speed images captured during a compression test in the normal direction at a strain rate of approximately 4000/s. Note the presence of a crack in the final three frames. The third frame corresponds to a strain level of approximately 0.2 which is a significant increase in strain-to-failure over quasi-static tests.

The total energy absorbed during deformation is an important factor under impact conditions. The AZ31B experimental results show that as the applied strain rate increased, the energy absorption increased in the normal direction but remained the same in the rolling and transverse directions. In the normal direction, the energy absorption was 10.7 MJ/m^3 at quasi-static rate and 34.1 MJ/m^{3}at high rates. In the rolling direction, the energy absorption was 21.9 MJ/m^3 at quasi-static rate and 20.1 MJ/m^{3}at high rates. In the transverse direction, the energy absorption was 23.4 MJ/m^3 at quasi-static rate and 25.9 MJ/m^3 at high rate.

Microstructural analysis was conducted on the specimens before and after each test and image analysis (Williams and Carino 2007) was conducted to calculate the particle size distribution, the particle nearest neighbor distance distribution, the aspect ratio distribution, and the total particle area fraction. The number and percentage of fractured particles was also determined. Each specimen was then etched so that grain size and twin density analysis could be performed.

Figure 3.4 shows optical microscope images of the polished and etched specimens. This particular specimen was oriented in the normal direction and tested in quasi-static compression. Image 4a consists of a mosaic of sixteen smaller images so that a representative area could be analyzed. The grain size, particle information, and twin information were each averaged from a total of nine separately analyzed images. Tables 1 and 2 summarize the results of the particle and twin/grain size analysis, respectively.

The role of twinning in the deformation of AZ31B is vital in understanding the mechanisms responsible for plasticity. In the quasi-static regime, the, flow stress curve for the normal direction is convex reflecting deformation mostly accommodated by slip along the basal and pyramidal planes similar to behavior reported for rolled magnesium by Kelley and Hosford (1968), Agnew and Duygulu (2005), and Lou et al (2007) as well as extruded magnesium as reported by Barnett (2004). Initial EBSD analysis showed a strong basal dominated texture such that most of the grains are oriented unfavorably with respect to the common tensile twin $\{10\bar{1}2\}$. This reduced activity of the tensile twin is further evidenced by the reduced twin density measured for the normal direction when compared to the rolling and transverse directions in Table 3.2.

DISCUSSION

The flow stress curves for loading along the rolling and transverse directions exhibit strong hardening behavior after an initial period of low strain hardening which has been ascribed in the literature to the influence of the substantial fraction of tensile twin on slip dislocation activity once slip overtakes twinning as the dominant plastic deformation mechanism (Barnett et al. 2004, Jain and Agnew 2007, and Lou et al. 2007).

In the high strain rate tests, trends similar to the quasi-static tests were observed, but the hardening degree was substantially increased for all loading orientations. For the specimens tested in the normal direction, the yield stress, elongation to failure and hardening rate increased dramatically. As suggested by Table 3.2, the increase of the yield stress and hardening rate could be attributed to more enhanced tensile twin activity. The increased activity was not significant enough to induce a sigmoidal curve, but may have been large enough to induce a noticeable effect on the interaction between twinning and slip dislocation activity. This phenomenon could increase the hardening rate by a mechanism similar to that correlated to the post-twin hardening effect observed for the rolling and transverse direction specimens.

The post twin-dominated hardening rate was significantly increased for both the rolling and transverse directions, but moreso for the transverse direction. This more pronounced increase in the transverse direction is further evidence of the effect of an intensified twinning-slip interaction and texture induced twinning in the high strain rate regime.

Table 3.1 shows that as the strain rate increased, the number density of fractured particles increased. This trend was similar to that found by Dighe et al. (2000) for an

aluminum alloy where fractured particles were quantified and related to the dominant fracture mechanisms. These trends indicate that the dominant mechanism for failure was void growth and coalescence. Decreasing strain-to-failure and increasing number density of fractured particles with increasing strain rate would indicate crack-void nucleation as the dominant mechanism. For more detailed discussions on the link between structural properties and damage mechanisms, refer to the works by Dighe et al (2000), Horstemeyer et al (2000), and Barbee et al (1972).

Table 3.2 summarizes the results from the twin and grain size examination. The twin density increased as the applied strain rate increased. In addition, the nearest neighbor distance of twins decreased as the strain rate increased. However, the twin length did not change as a function of applied strain rate. This was also true of the grain size. The observed correlation between the grain size and twin length suggests that the twin length may be governed by grain size and may be insensitive to loading direction or strain rate.

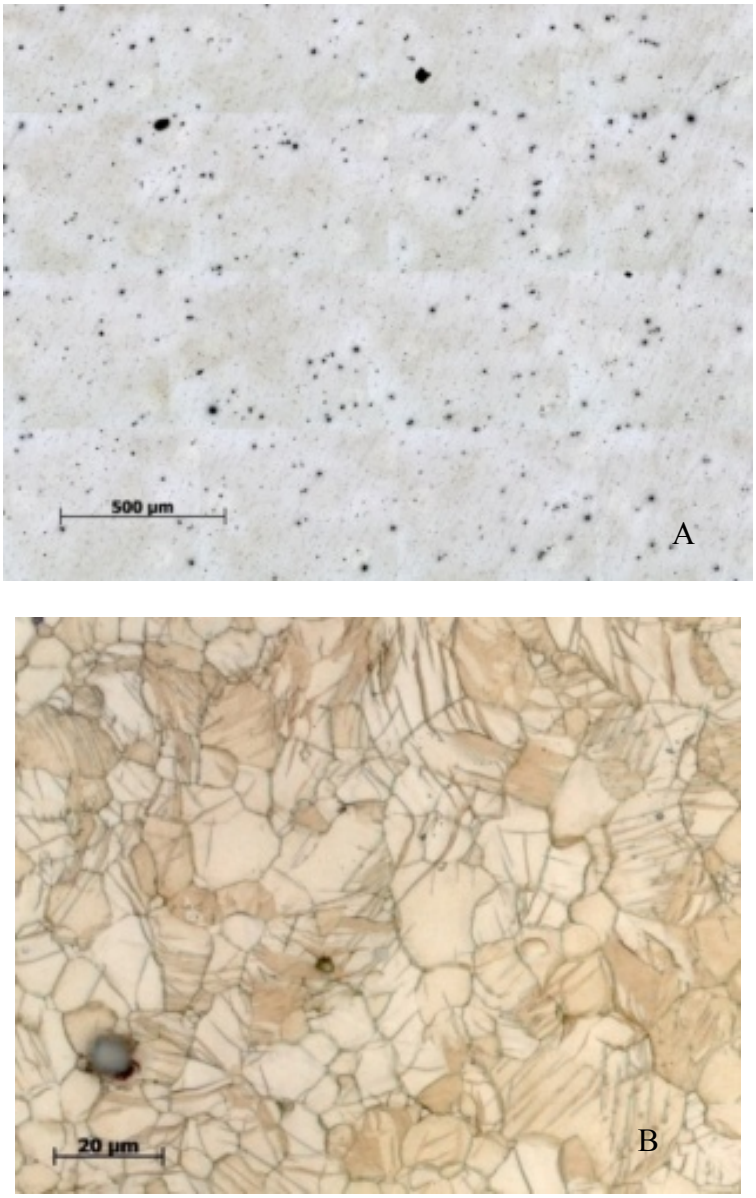

Figure 3.4**.** Specimen images after quasi-static compression orientated in the normal direction. Figure 3.4a shows after polishing and before etching to allow for the characterization of the parameters related to the second-phase particles. Figure 3.4b shows the same specimen after etching with grain boundaries and deformation twins evident. Note the variation in scale.

Table 3.1. Results of the particle analysis (ND=normal direction, TD=transverse direction, RD=rolling direction, QS=quasi-static test, HR=high rate test, SD=standard deviation, NND=nearest neighbor distance).Orientations of testing and miocrostructural analysis relative to the as-received AZ31B plate.

	Particle Size		Particle NND		Particle Aspect Ratio		Particle Area Fraction (%)	Fractured Particles/ mm^2
	Mean (μm)	SD	Mean (μm)	SD	Mean	SD		
ND Untested	5.6	3.6	29	17	1.9	0.94	0.96	2.2
ND QS Tested	6.4	4.2	29	17	1.8	0.78	1.40	4.3
ND HR Tested	5.1	2.6	13	6.8	1.8	0.64	3.90	9.3
TD Untested	6.8	4	19	9.4	1.7	0.55	3.80	3.7
TD QS Tested	8.2	7.1	25	15	1.7	0.87	3.20	4.3
TD HR Tested	4.4	3.8	17	14	1.9	0.95	1.32	8.4
RD Untested	5.6	2.4	25	17	1.9	0.83	0.85	4.2
RD QS Tested	3	3.2	17	15	1.9	0.94	0.80	5.0
RD HR Tested	3.7	5	20	19	2	1.1	1.10	8.4

Table 3.2. Results of the twin and grain size analysis (ND=normal direction, TD=transverse direction, RD=rolling direction, QS=quasi-static test, HR=high rate test, NND=nearest neighbor distance).

	Average Grain Size (μm)	Twin Density (twins/100 μm^2)	Normalized Twin Density	Average Twin Length (μm)	Average Twin NND (μm)
ND Untested	12.5	1.6	1	6.1	1.6
ND QS Tested	9.1	3.7	2.3	7.5	1.9
ND HR Tested	8.8	6.4	3.9	4.4	1.4
TD Untested	12.6	1.5	1	8.1	2.4
TD QS Tested	10.3	6.1	4.1	5.5	1.5
TD HR Tested	8.4	9.6	6.4	5.9	1.3
RD Untested	12.0	1.7	1	6.8	2.1
RD QS Tested	10.3	5.3	3.2	4.8	1.6
RD HR Tested	9.6	9.1	5.5	4.2	1.2

CONCLUSIONS

Based on the results of this study, the following conclusions were observed:

1. Energy absorption increased with an increased strain rate in the normal direction while the energy absorption in the rolling and transverse directions were within the level of testing uncertainty.
2. The level of strain-to-failure increased as the strain rate increased in the normal direction; however, the strain-to-failure slightly decreased in the rolling and transverse directions as the strain rate increased.

3. The twin density and fractured particle density increased as the strain rate increased in all three orientations.
4. Based on increasing number density of fractured particles and increased strain-to-failure with increasing strain rate, void growth and coalescence are the dominant fracture mechanisms.
5. The texture of the material played a significant role in the plastic deformation at both quasi-static and high strain rates due to twin-slip interactions.

REFERENCES

Agnew, S.R. and Duygulu, Ö., Int. J. Plast., 21 (2005) 1161

Barbee, T.W., Seaman, L., Crewdson, R., and Curran, D., J. Mater., JMLSA 7 (3) (1972) 393

Barnett, M.R., Keshavarz, A., Beer, A.G., and Atwell, D., Acta Mat., 52 (2004) 5093

Dighe, M.D., Gokhale, A.M., Horstemeyer, M.F., and D.A. Mosher, D.A., Met. Trans. A, V 31A, (2000) 1725

Gary, G., DAVID Manual, (2005), http://www.lms.polytechnique.fr/dynamique/greef/web4034_david.html

Horstemeyer, M.F., Lathrop, J., Gokhale, A.M., and Dighe, M., Theoretical and Applied Fracture Mechanics, V 33, Issue 1, (2000) 31

Ishikawa, K., Watanabe, H., and Mukai, T., J. Mat. Sci., 40 (2005a) 1577

Ishikawa, K., Watanabe, H., and Mukai, T., Mat. Letters, V59, 12, (2005b) 1511

Jain, A., and Agnew, S.R., Mat. Sci. Eng. A., V 462, special Issue, (2007) 29

Kelley, E.W. and Hosford, H.F., Trans. Metall. Soc. AIME 242 (1968) 654

Kim, H.K. and Kim, W.J., Mat. Sci. Eng. A, 385 (2004) 300

Livescu, V., Cady, C.M., Ceretta, E.K., Henrie, B.L., and Gray, G.T., "The high strain rate deformation behavior of high purity magnesium and AZ31B magnesium alloy." A. A. Luo, N. Neelameggham, R. Beals, eds, Magnesium Technology, TMS, Warrendale, PA (2006)

Lou, X.Y., Li, M., Boger, R.K., Agnew, S.R., and R.H. Wagoner, R.H., Int. J. Plast., 23 (2007) 44

Mukai, T., Yamanoi, M., and Watanabe, H., Met. Trans. V 42, 7 (2001) 1177

Mukai, T., Watanabe, H., and Ishikawa, K., Magnesium alloys 2003, V419-4 (2003) 171

Williams, T.N., and Carino, R.L., (Nov 2007), "ImageAnalyzer - A Software Tool for Calculating Certain Material Model Constants from Optical Images", CAVS Internal Report

CHAPTER IV

THE EFFECT OF VARYING STRAIN RATES AND STRESS STATES ON THE PLASTICITY, DAMAGE, AND FRACTURE OF ALUMINUM

INTRODUCTION

Understanding material behavior and associated failure mechanics is pivotal in the development of reliable and safe yet lightweight structural components for a myriad of engineering applications. For lightweight design, aluminum alloys have been used extensively for their stiffness and strength-to-weight ratios. The growing applications of aluminum alloys in both the aerospace and automotive industries have brought great challenges manifested in understanding material behavior from the quasi-static regime to the high rate regime. In this study, we aim to quantify material behavior and associated failure mechanics of three aluminum alloys commonly used in automotive, aerospace, and defense applications from quasi-static to fairly high strain rates. In quantifying material behavior and the associated damage progression and fracture, we focused on a cast A356-T6 aluminum alloy, an extruded 6061-T6 aluminum alloy, and a rolled 5083-H131 aluminum alloy. A theoretical modeling and experimental study showed the stress state differences in the stress-strain behavior was real in Horstemeyer et al. (2000a) for the A356 aluminum alloy. In this study, the stress level differences reach up to 30% different depending on the strain level. To date, no study has been performed under

tension, compression, and torsion at different strain rate levels according to the authors' knowledge. As such, quantifying these effects and evaluating models to see if they can capture this effect would be useful, if higher quality simulation-based design and analysis were to be realized. Engineering applications of such behavior include any high strain rate applications, such as crashworthiness, impact, penetration, or military scenarios.

One theoretical key to understanding the mechanical response of materials under different stress state and strain rates is the damage evolution and fracture characteristics. Garrison and Moody (1987) gave a general review of ductile fracture for many different metal alloys with the trends being pertinent for aluminum. Essentially, ductile fracture arises from damage nucleation stemming from particle fracture or particle/matrix debonding (Goods and Brown, 1979), voids growing from these nucleation sites, and voids coalescencing after their growth has initiated (Horstemeyer et al., 2000b,c, 2007). The idea to describe material ductile failure due to nucleation, growth, and coalescences has led to the appearance of many mathematical formulations. As mentioned earlier, Horstemeyer and Gokhale (1999) developed a damage nucleation model that accounted for the stress state dependence and applied it to aluminum alloy A356 aluminum alloy. For aluminum alloys, Gokhale and co-workers have studied different nucleation damage progression for different aluminum alloys under quasi-static loading conditions. Under quasi-static loading, Dighe et al. (1998) found that as the temperature increased, the void nucleation rate decreased for an A356 aluminum alloy. They concluded in Dighe et al. (2000) that the A356 aluminum alloy does not have a significant strain rate dependence on the damage nucleation and also quantified the stress state dependence of the damage nucleation as tests were conducted under tension, compression, and torsion for an A356

aluminum alloy (Dighe et al., 2002). One might think that since there was a clear temperature dependence on the damage nucleation, that the applied strain rate would give an inverse relationship due to dislocations and associated work hardening operating in that fashion. However, for the high rate tests, the temperature is not isothermal due to heat generation arising from plastic work. As such, clearly distinguishing the temperature and strain rate effects apart from each other is difficult under these high rate conditions. Balasundaram et al. (2002) quantified the damage nucleation of a 5086 aluminum alloy under compression, and Agarwal et al. (2002a) studied the damage nucleation of a 6061-T6 aluminum alloy under compression. Agarwal et al. (2002b) also studied the damage nucleation of a 6061-T6 aluminum alloy under tension and compared the results with their compression data. These particular studies occurred under quasi-static strain rates, and no torsion was examined. A good review of quasi-static material behavior for aluminum alloys can be found in Jordon (2007).

High rate compression tests have been previously performed on A356-T6 (Dighe et al., 2000). For 6061-T6 aluminum alloy, Kapoor and Nemat-Nasser performed high strain rate compression tests, and Lindholm et al (1971), Nicholas (1981), and Staab and Gilat (1991) performed high strain rate tension tests. High strain rate torsion testing of any of the alloys was not found in the literature; as such, the comparison of high strain rate, stress state dependent stress-strain behavior is lacking in the literature. There is precious little information on 5083-H131 aluminum alloy as well. Although several studies have shown some strain rate dependence of aluminum alloys on the stress state and work hardening, none have shown a systematic study on the varying strain rates with varying stress states (compression, tension, and torsion) with different alloys. In our

study, we conduct experiments and performed micro-structural analysis to quantify the structure-property relationships and the associated damage nucleation for three ductile aluminum alloys by examining the stress-strain behavior under different applied strain rates and stress states. In this context, we employ the Horstemeyer and Gokhale (1999) void-crack nucleation model to help provide a theoretical basis for our experimental results.

MATERIAL PROPERTIES

Three different aluminum alloys were examined in this study: 5083 in the H131 condition, A356 in the T6 condition, and 6061 in the T6 condition. These three alloys represent three different materials processing methods: the 5083-H131 was rolled, the 6061-T6 was extruded and then heat treated, and the A356-T6 was cast and heat treated. Specimens from the 5083-H131 aluminum alloy were retrieved from the rolling direction; specimens from the 6061-T6 aluminum alloy were retrieved from the extruded direction. The 5083-H131 was heavily alloyed with magnesium and manganese. The secondary particles composed of $Al_6(Fe,Mn)$ contribute to 1.1% of the total surface area. These particles are an average of 4.1 microns in diameter and have an average nearest neighbor distance of 20 microns as shown in Table 4.2. The 6061-T6 aluminum alloy is heavily alloyed with magnesium as well but has more silicon than does the 5083-H131 aluminum alloy. The secondary particles consist of Mg_2Si and AlFeSi and contribute less than 1% of the total surface area. The 6061-T6 secondary particles averaged 1.3 microns in diameter with an average nearest neighbor distance of 11.4 microns. Since 6061-T6 is precipitate hardened many smaller particles in the size range of 50-200 nanometers were

present. These particles were not visible on the optical micrographs but were observed at the base of the small voids on the fracture surfaces. The A356-T6 aluminum alloy is most heavily alloyed with silicon as shown in Table 4.1. These silicon rich particles contributed 7.3% of the total surface area, much more than the particles in either the 5083-H131 or 6061-T6 aluminum alloys. The average particle size was slightly larger than that of 5083-H131 aluminum alloy at 6 microns, but had a much smaller nearest neighbor distance of 6.9 microns due to the increased number density.

Table 4.1. Chemical compositions of the three aluminum alloys.

	Al (%)	Cr (%)	Cu (%)	Fe (%)	Mg (%)	Mn (%)	Si (%)
5083-H131	92.4-95.6	0.05-0.25	< 0.1	<0.4	4-4.9	0.4-1.0	<0.4
6061-T6	95.8-98.6	0.04-0.35	0.15-0.40	< 0.7	0.8-1.2	<0.15	0.4-0.8
A356-T6	91.1-93.3	N/A	<0.2	< 0.4	0.25-0.45	<0.1	6.5-7.5

Table 4.2. Particle size, nearest neighbor distance, aspect ratio, area fraction, and fractured particle statistics for the as-received specimens.

	Particle Size		Particle NND		Particle Aspect Ratio		Particle Area Fraction (%)
	Mean (µm)	SD (µm)	Mean (µm)	SD (µm)	Mean (µm)	SD (µm)	
5083-H131	4.3	2.9	20	14	1.64	0.65	1.1
6061-T6	1.3	0.7	11.4	8.3	2.3	1.0	0.85
A356 T6	6.0	1.7	6.9	2.8	2.4	1.5	7.3

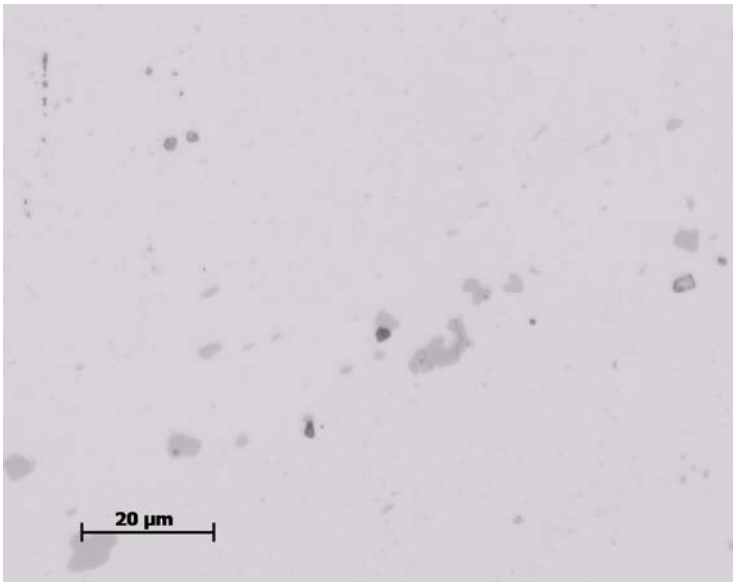

Figure 4.1. Optical microscope image of a 5083-H131 aluminum alloy in the as-received condition with $Al_6(Fe,Mn)$ secondary particles evident. The rolling direction is perpendicular to the image.

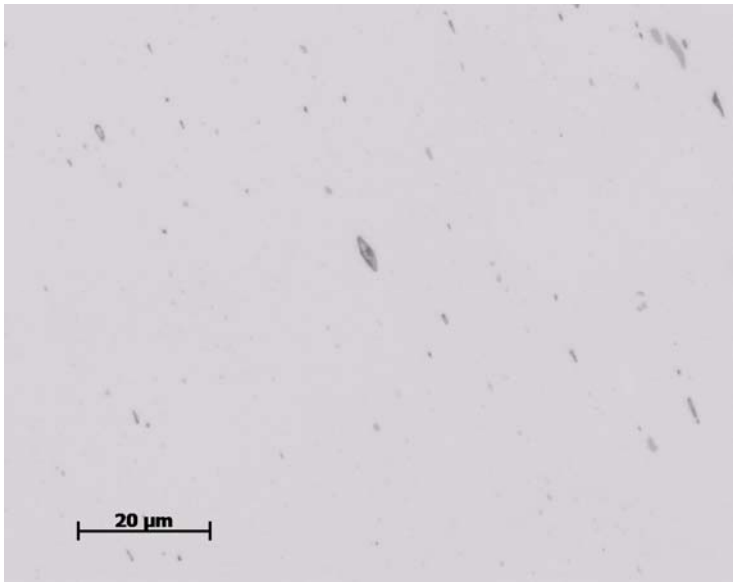

Figure 4.2. Optical microscope image of a 6061-T6 aluminum alloy specimen in the as-received condition with Mg_2Si and AlFeSi secondary particles evident. The extrusion direction is perpendicular to the image.

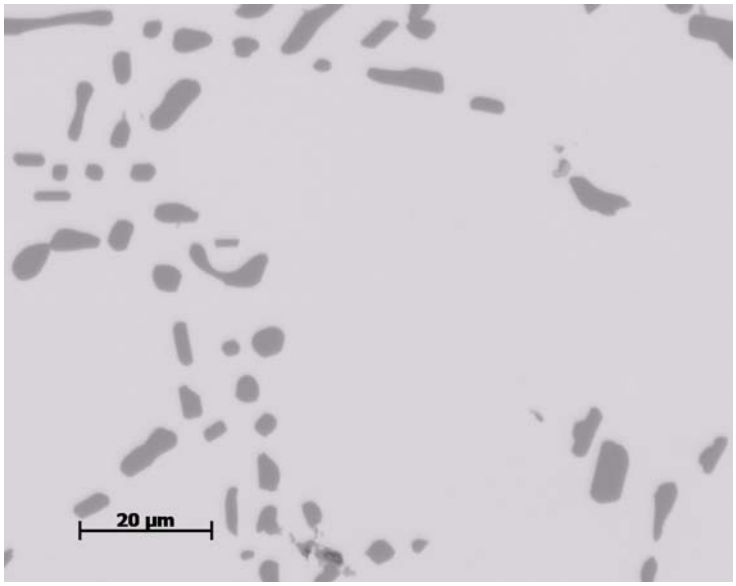

Figure 4.3. Optical microscope image of a cast A356-T6 aluminum alloy specimen in the as-received condition with silicon particles evident.

EXPERIMENTAL PROCEDURES

To quantify the stress-strain behavior under different stress states and applied strain rates, different testing methods of ascertaining the data was warranted. The quasi-static tension and compression tests were performed on an Instron electro-mechanical testing machine. The torsion tests were performed using an MTS multi-axial servo-hydraulic test system. The high rate testing was performed using various split Hopkinson bars based on the work by Hopkinson (1904) and Kolsky (1949).

The high rate compression tests were carried out using a split Hopkinson pressure bar (Kolsky) apparatus with the striker, incident, and transmitted bars all consisting of maraging steel 12.5 mm in diameter. The high strain rate compression data was analyzed using the DAVID software package (Gary, 2005). The specimens were generally not tested to failure. Force equilibrium between the two faces of each specimen was

validated using the software and good agreement was found. All strain rates were calculated as the best linear correlation of a strain versus time plot from a strain level of 0.02 to the end of the data. The strain rate was then rounded to the nearest 100/s.

The high strain rate tension tests were performed using a direct tension Hopkinson bar similar to that outlined by Staab and Gilat (1991). The tension bar uses a clamped section of the incident bar to induce a tensile wave that is released by breaking a pin in the clamp and the signals are measured at three locations, near the center of the incident bar past the breaker pin, near the end of the incident bar and specimen, and just past the specimen on the transmitted bar, instead of the traditional two locations for compression tests. The analysis method was modified by including the effect of dispersion on the tensile wave by incorporating the work of Bancroft (1941) similar to the method employed by Zhao and Gary (1997) and Bussac et al. (2002). The waves are first converted to the frequency domain using a Fast Fourier Transform and then shifted to the proper locations for analysis using the DAVID software package. This allowed for the advantages of using DAVID for analysis including the verification of force equilibrium, which is especially important for tension, because of the small level of plasticity before fracture initiation. All of the tension specimens were tested to failure and the strain rates were calculated in the same manner as the compression tests.

The high strain torsion tests were performed using a torsional Hopkinson bar developed after Gilat and Wu (1994). The torsion bar construction is similar to that of the tension bar in that a clamped section of the incident bar is used to induce a shear wave that is released when a breaker pin in the clamp is broken. The torsion test data were analyzed in the same manner as laid out by Gilat and Wu (1994).

All of the specimens were polished post-mortem and optical micrographs were taken at magnifications of 500x-1000x, depending on the level needed to ascertain the relevant damage characteristics. In particular, the damage nucleation progression (from particle fracture and particle/matrix debonding) depended heavily on the particle size. The number density of fractured and/or debonded particles was counted manually as a significant number of sample images is warranted to obtain representative results. For the tension and torsion specimens, fractured and debonded particles were counted, but for compression specimens no debonded particles were present so all the results for compression tests corresponded to fractured particles.

EXPERIMENTAL RESULTS

Figures 4.4 - 4.6 show the stress-stain behavior of the 5083-H131, A356-T6, and 6061-T6 aluminum alloys from the different stress state and applied strain rate tests. For consistency of results, the torsion test data were converted to effective stress and effective strain for comparison with the tension and compression data. Table 4.3 summarizes the stress state and strain rate effects on the flow stress at an effective strain level of 0.06. As shown in Figures 4a and 4b for the 5083-H131 aluminum alloy, compression gave the greatest work hardening and torsion incurred the lowest work hardening. As anticipated, the stress state increased with an increased applied strain rate. The error bands signify that the testing variation was small enough that these trends are true phenomena. The A356-T6 aluminum alloy, as illustrated in Figures 5a and 5b, followed the same trend as the 5083-H131 aluminum alloy in terms of the work hardening being greater for the compression and lowest for torsion. Figures 6a and 6b show that for the 6061-T6

aluminum alloy that the trends are very different. Although compression incurred the greatest work hardening rate, tension, not torsion, incurred the lowest work hardening rate. Also, Figures 6a and 6b show a similar trend as the 5083-H131 aluminum alloy in that as the applied strain rate increased, the associated stress level increased. Table 4.3 summarizes the stress state and strain rate effects on the flow stress at an effective strain level of 0.06.

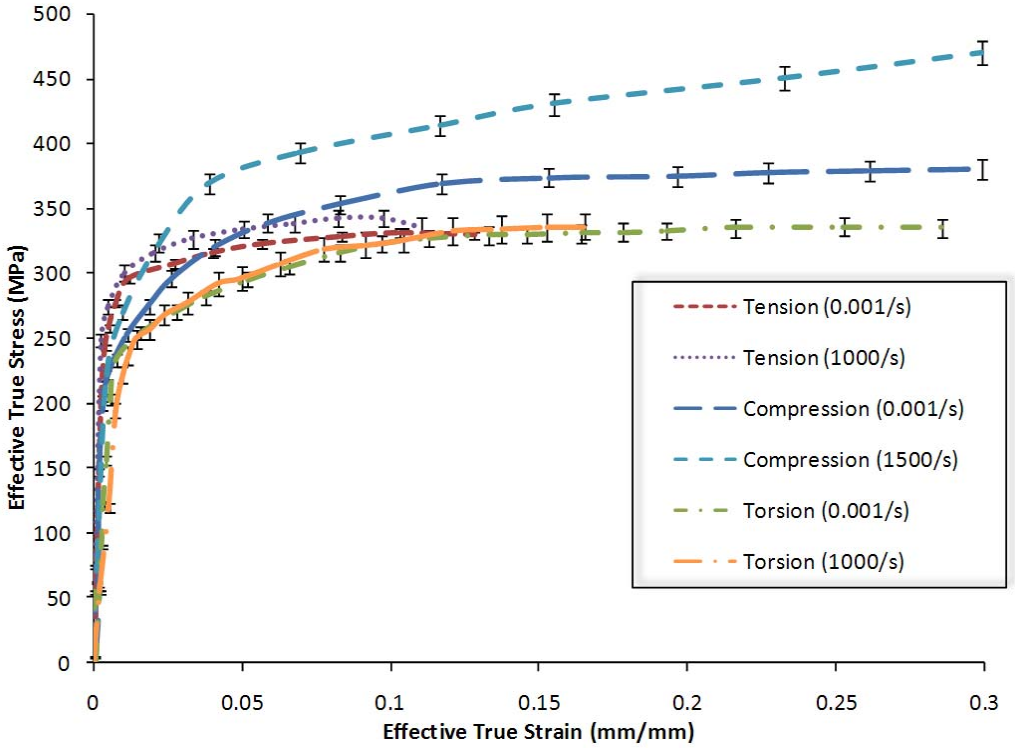

Figure 4.4a. Effective stress-strain curves of 5083-H131 aluminum alloy tested in the rolling direction under varying stress states and strain rates showing effects on the resulting plasticity. The error bars indicate the variation present among three tests.

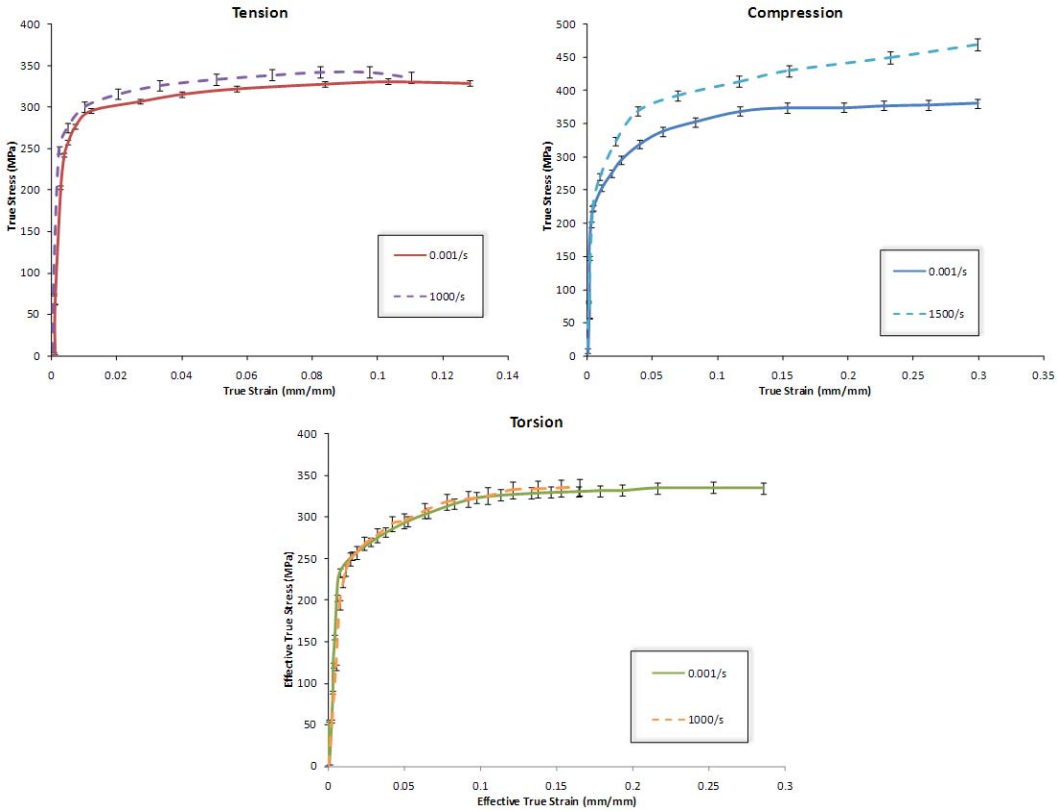

Figure 4.4b. Stress-strain data of 5083-H131 under varying strain rates separated by stress state.

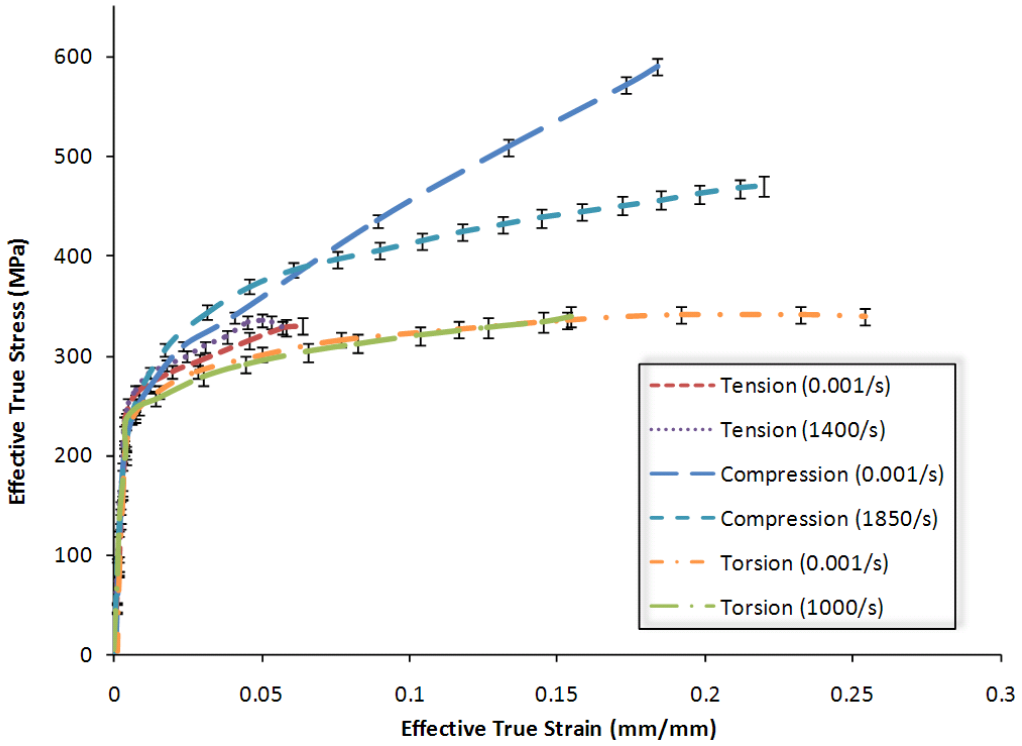

Figure 4.5a. Effective stress-strain curves of the A356-T6 aluminum alloy tested under varying stress states and strain rates showing effects on the resulting plasticity. The error bars indicate the variation present among three tests.

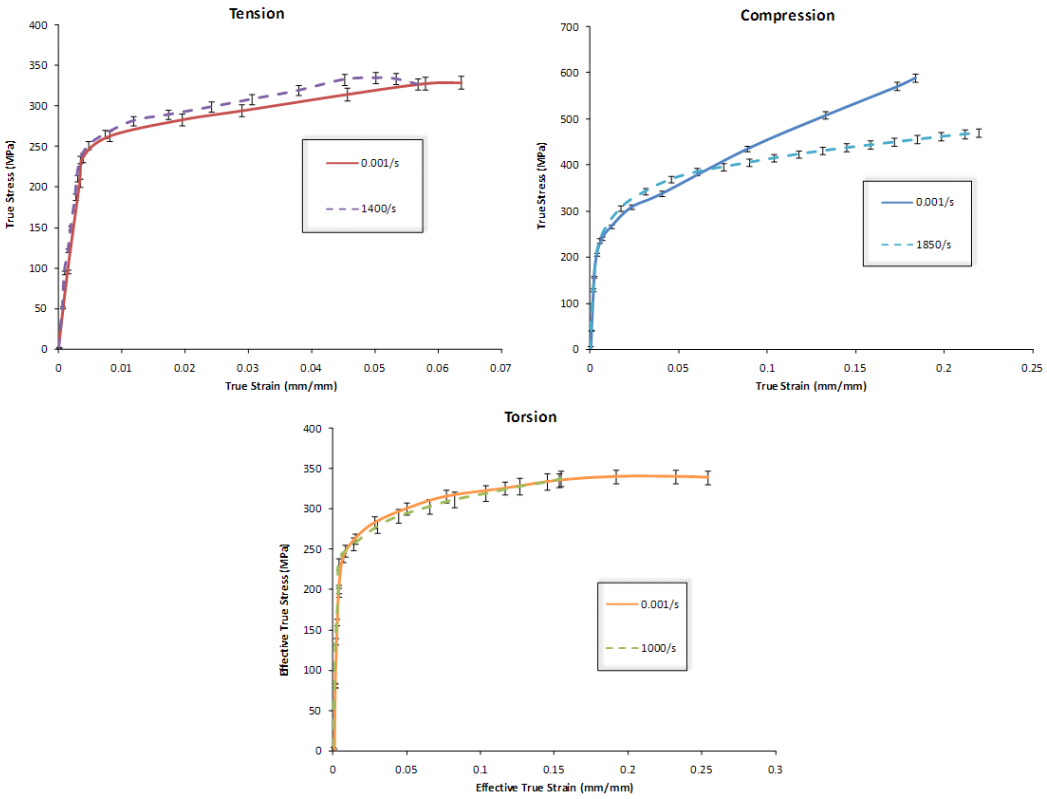

Figure 4.5b. Stress-strain data of A356-T6 under varying strain rates separated by stress state.

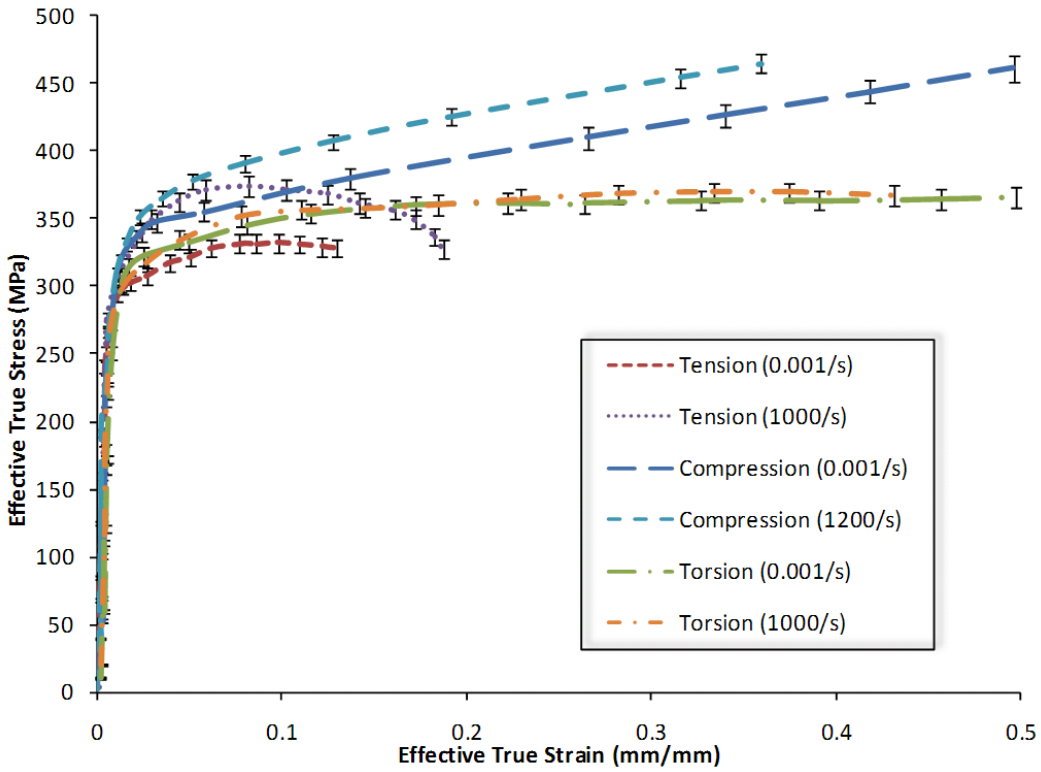

Figure 4.6a. Effective stress-strain curves of 6061-T6 aluminum alloy tested in the rolling direction under varying stress states and strain rates showing effects on the resulting plasticity. The error bars indicate the variation present among three tests.

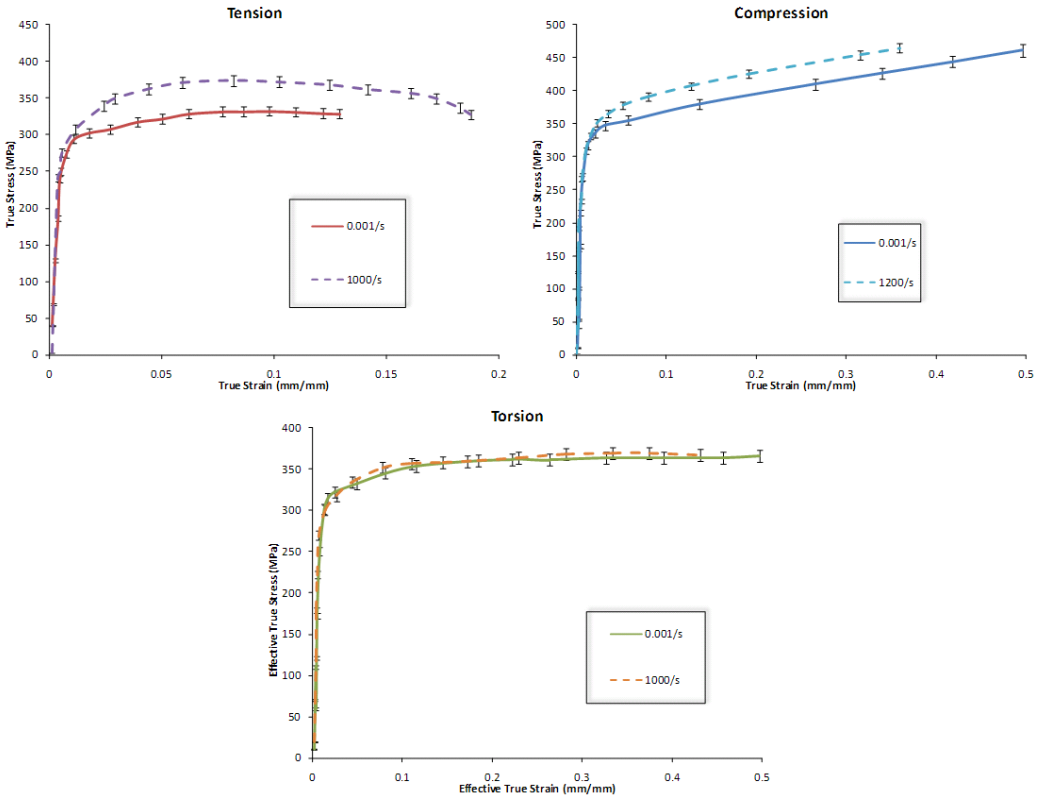

Figure 4.6b. Stress-strain data of 6061-T6 under varying strain rates separated by stress state.

Table 4.3. Comparison of flow stress at 6% effective strain and the resulting stress state and strain rate effects for each of the alloys. Stress state effect is calculated as the percent difference between the flow stress at the same strain rate but under different stress states with tension as a benchmark. The strain rate difference is calculated as the percent difference between the flow stress under the same stress state but varying strain rates.

		5083-H131			6061-T6			A356-T6		
		Flow Stress (MPa)	Effect of the Stress State on the Flow Stress (%)	Effect of the Strain Rate on the Flow Stress (%)	Flow Stress (MPa)	Effect of the Stress State on the Flow Stress (%)	Effect of the Strain Rate on the Flow Stress (%)	Flow Stress (MPa)	Effect of the Stress State on the Flow Stress (%)	Effect of the Strain Rate on the Flow Stress (%)
TENS	QS	323	Normalizing value	N/A	328	Normalizing value	Normalizing value	329	Normalizing value	Normalizing value
	HR	335	Normalizing value	4 ↑	371	Normalizing value	13 ↑	327	Normalizing value	1 ↓
COMP	QS	340	5 ↑	Normalizing value	356	9 ↑	Normalizing value	378	14 ↑	Normalizing value
	HR	386	15 ↑	14 ↑	382	3 ↑	7 ↑	385	16 ↑	2 ↑
TOR	QS	301	7 ↓	Normalizing value	337	3 ↑	Normalizing value	310	20 ↓	Normalizing value
	HR	305	9 ↓	1 ↑	343	8 ↓	2 ↑	300	25 ↓	3 ↑

POST-MORTEM MATERIAL CHARACTERISTICS

After testing the specimens were polished perpendicular to the loading plane so that microscopic imaging could be performed. Scanning electron microscope images were taken from the tensile specimen fracture surfaces. Figures 7-9 show the fracture surfaces for the different aluminum alloys in tension at different applied strain rates (0.0001/s and ~1000/s). The number density of fractured and debonded particles was quantified from optical microscopic images of the polished surfaces, and the data was correlated to the nucleation model developed by Horstemeyer and Gokhale (1999) as shown in Figures 10-12. The model parameters are given in the Discussion section. The number density of voids on the tensile fracture surfaces were quantified, and the differences between the quasi-static and high strain rates were tabulated as shown in Table 4. The areas analyzed

were chosen as being the nearest to a flat surface. The voids were also categorized into large and small voids with the differentiating size being the mean particle size for each material. The minimum detectable void size differed among the alloys due to the differences in magnification used for the analyses.

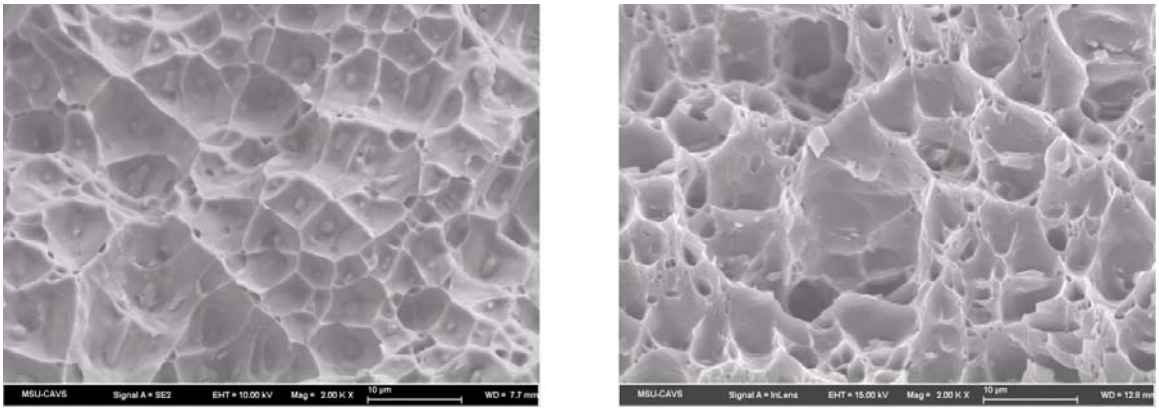

Figure 4.7. Fracture surfaces of 5083-H131 aluminum alloy under tension at two different applied strain rates (a) 0.0001/s on the left and (b) ~1000/s on the right.

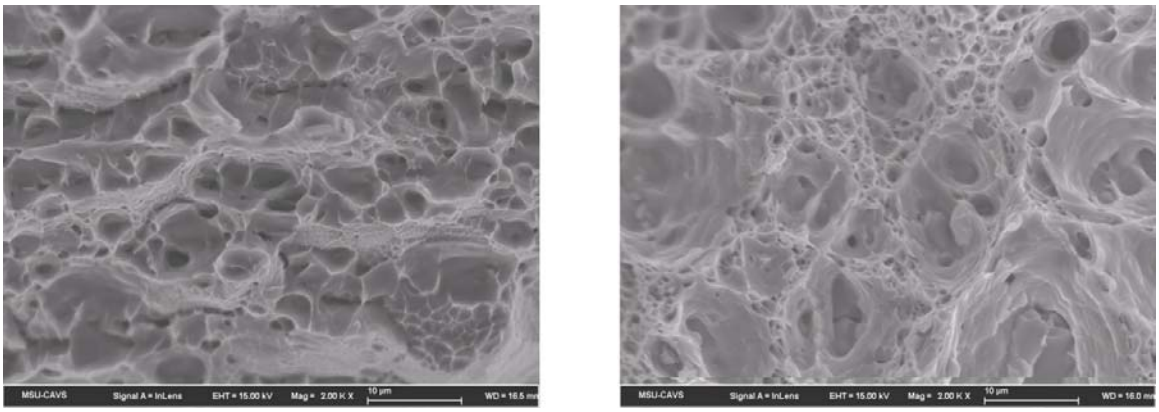

Figure 4.8. Fracture surfaces of 6061-T6 aluminum alloy under tension at two different applied strain rates (a) 0.0001/s on the left and (b) ~1000/s on the right.

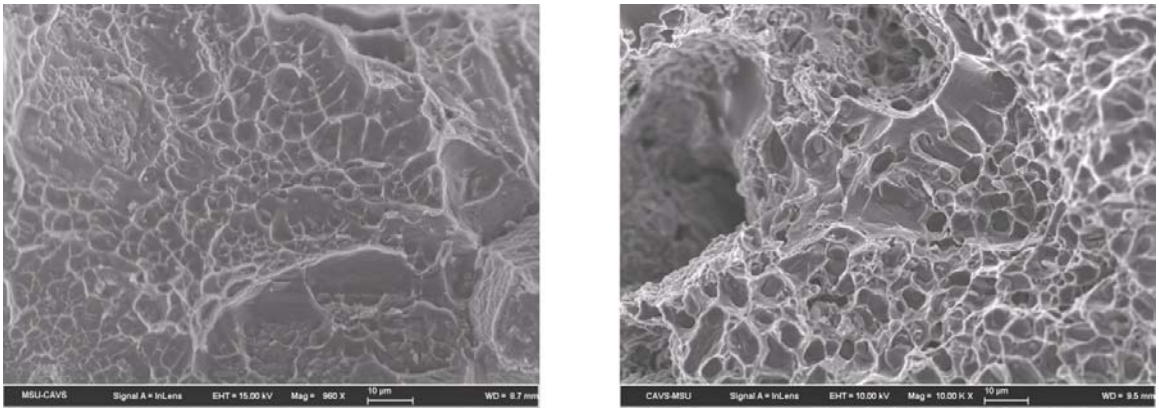

Figure 4.9. Fracture surfaces of A356-T6 aluminum alloy under tension at two different applied strain rates (a) 0.0001/s on the left and (b) ~1000/s on the right.

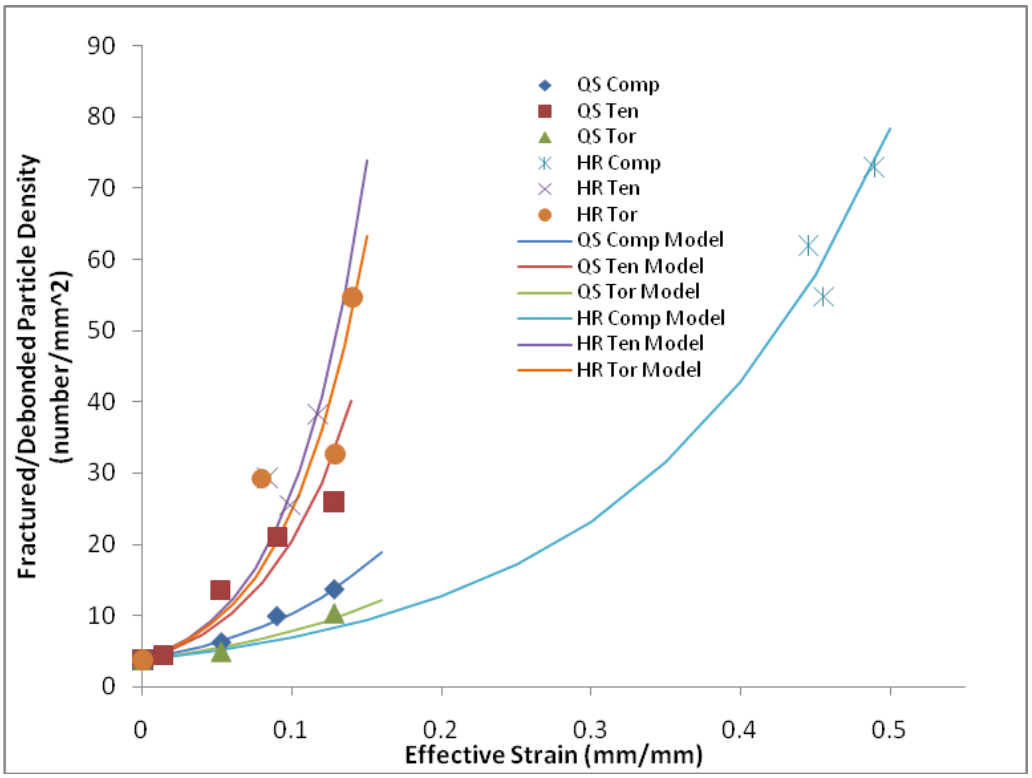

Figure 4.10. Void nucleation (number density) versus strain comparing the experimental data and Horstemeyer-Gokhale model under varying stress states and strain rates for 5083-H131 aluminum alloy.

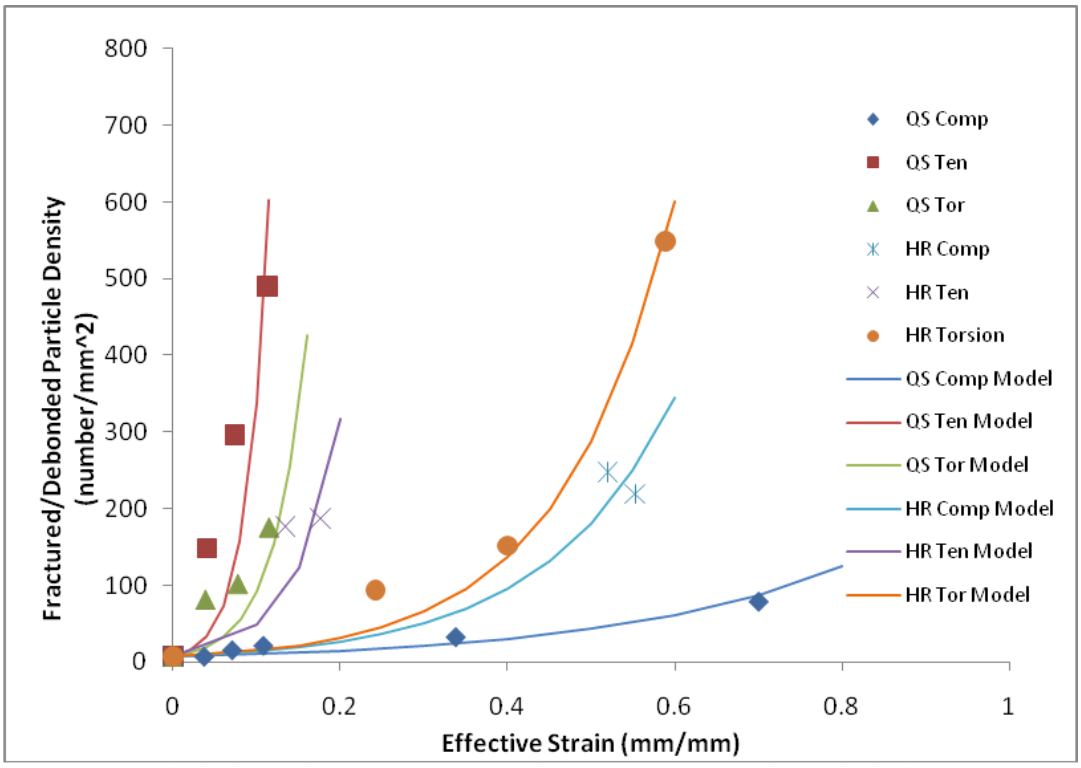

Figure 4.11. Void nucleation (number density) versus strain comparing the experimental data and Horstemeyer-Gokhale model under varying stress states and strain rates for 6061-T6 aluminum alloy.

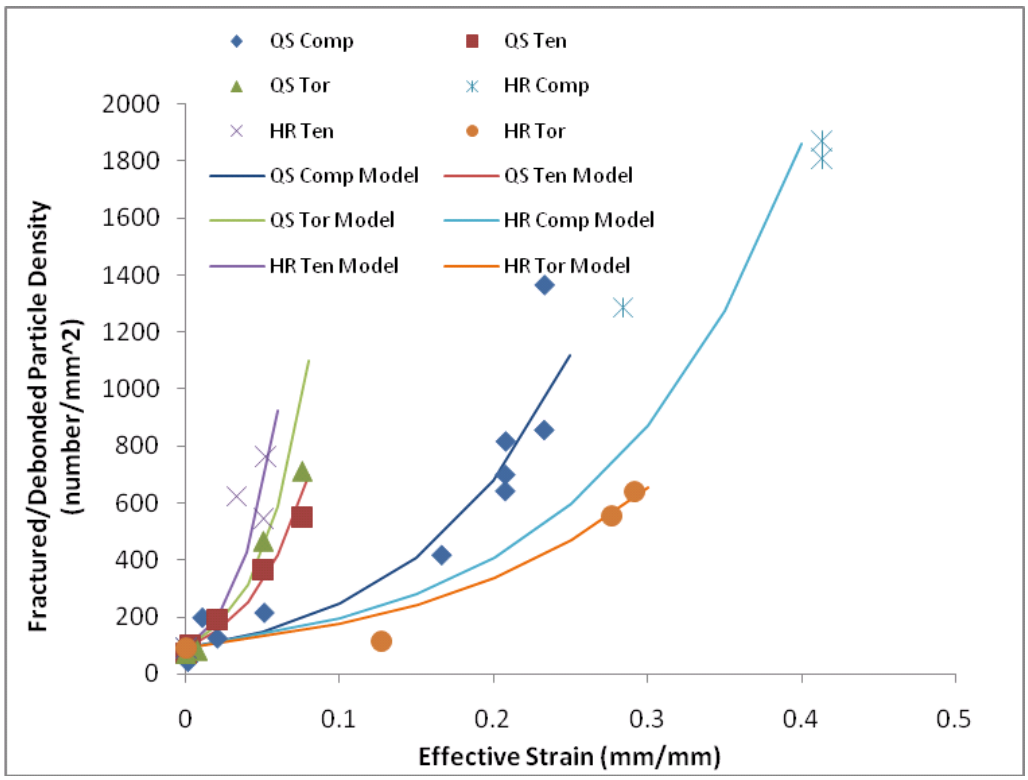

Figure 4.12. Void nucleation (number density) versus strain comparing the experimental data and Horstemeyer-Gokhale model under varying stress states and strain rates for A356 aluminum alloy.

Table 4.4. Void number density present on tensile fracture surfaces.

		Void Density ($1/mm^2$)	Effect of the Strain Rate on the Void Density (%)	Percentage of Small Voids to Total Number of Voids (%)	Effect of the Strain Rate on the Percentage of Small Voids (%)	Minimum Detectable Void Size (mm^2)
5083-H131	QS	8.32E+04	Normalizing value	35	Normalizing value	0.13
	HR	1.36E+05	62 ↑	59	24 ↑	
6061-T6	QS	1.72E+05	Normalizing value	39	Normalizing value	0.13
	HR	2.36E+05	58 ↑	98	61 ↑	
A356-T6	QS	3.23E+04	Normalizing value	58	Normalizing value	0.6
	HR	4.52E+04	58 ↑	63	5 ↑	

DISCUSSION

Several clear trends can be observed from this complex set of data. First, the stress state dependence of the void-crack nucleation is inversely tied together with the associated work hardening rates. Therefore, as the void-crack nucleation rate decreased, the work hardening rate increased relatively. For example, the void-crack nucleation for tension was greater than compression, but the compression stress-strain behavior was greater from compression than for tension.

A second trend as observed from Table 4.4 is that as the applied strain rate increased, the number density of voids increased approximately 60% on the fractured tensile specimen surfaces for all three materials. This indicates that the nucleated voids had less time to grow at the higher strain rates and voids nucleated homogeneously throughout the specimen because of higher local stresses.

A third trend related to the tensile fracture surfaces that was observed was related to the different void-crack nucleation rates exhibited by the different materials. As observed from Table 4.4, the 6061-T6 aluminum alloy showed more smaller voids on the fracture surface arising from the precipitates than the larger particles as the strain rate increased. 98% of the voids were smaller for the high rate specimens, while only 39% of the voids were smaller for the low rate specimens. Although the void nucleation rate increased for the smaller voids for the other two aluminum alloys, the total values were much lower (59% to 35% for 5083-H131 and 63% to 58% for A356-T6). Clearly, the precipitates played a very crucial role in the failure process of the 6061-T6 aluminum alloy. Also related to this phenomena of two separate void nucleation rates arising from the precipitates and second phase particles is the elongation to failure increased for the

6061-T6 aluminum alloy but decreased for the 5083-H131 and A356-T6 aluminum alloys as the strain rate increased. The 6061-T6 aluminum alloy had an elongation to failure of 12.9% for low rate but 18.5% for high rate; the A356-T6 aluminum alloy had an elongation to failure of 6.4% for low rate but 5.7% for high rate; and the 5083-H131 aluminum alloy had an elongation to failure of 12.8% for low rate but 11.0% for high rate. Essentially, when the larger micron scale particles are prevalent in nucleating voids, the elongation to failure decreases as the applied strain rate increases. On the other hand, when the smaller nanoscale precipitates are prevalent in nucleating voids, the elongation to failure increases as the applied strain rate increases. Interestingly for torsion, the nucleation rates were nearly strain rate independent for 5083-H131 and A356-T6 but showed a decrease with increasing strain rate for 6061-T6. This is possibly related to the precipitate influence on the local stress state for void nucleation as well.

Along with some clear trends, there are some rather confusing trends as well. For example, for the A356-T6 and 5083-H131 aluminum alloys under compression showed an increase in the void nucleation rate under quasi-static deformation when compared to high rate deformation as shown in Figure 4.10. Although the uncertainty in the data might indicate that no difference is really observed, the opposite trend was exhibited for tension and torsion deformation cases. Finally, the highest void nucleation rates to the lowest occurred in tension followed by torsion and compression for all three materials at all the strain rates except the two compression just mentioned and the high rate torsion for the A356-T6 and 6061-T6 aluminum alloys. These confusing trends might be caused by effects arising from each material's texture, grain size, cohesive properties of the particle-matrix interfaces, and materials processing residual stresses.

In order to use the data for design and/or analysis, finite element analysis employing a constitutive model must be able to admit such data. Horstemeyer et al. (2000) employed the Horstemeyer-Gokhale (1999) void nucleation model to capture such behavior under quasi-static conditions for the A356 aluminum alloy. In the current study, we applied the Horstemeyer-Gokhale void-crack nucleation model for the varying strain rate data from the 5083-H131, 6061-T6, and A356-T6 aluminum alloys as illustrated in Figures 10-12. The material model constants for the nucleation model are given in Table 4.5.

Table 4.5. Material constants for the void nucleation model.

	5083-H131		6061-T6		A356-T6	
	Quasi-Static	High Strain Rate	Quasi-Static	High Strain Rate	Quasi-Static	High Strain Rate
C_{coeff}	3.75	3.75	7.25	7.25	90	90
a (GPa)	228	568	892	254	615	130
b (GPa)	41	80	235	84	586	118
c (GPa)	36	33.5	63	38	30	39
d (micron)	4.3		1.3		6	
f (%)	1		0.85		7	
K_{IC} (MPa $m^{1/2}$)	43		29		17.3	

SUMMARY

This study shows unprecedented experimental data revealing different flow stress and fracture characteristics under different deformation paths (tension, compression, and torsion). This stress state difference for the plasticity and damage evolution is exacerbated at different strain rates. Three different aluminum alloys (5083-H131, A356-T6, and 6061-T6) that had been processed in three different manners (rolling, casting, and extrusion respectively) were used to quantify the stress state differences under varying strain rates. Microstructural analysis was performed that quantified the void nucleation rates of three alloys as a function of stress state, strain rate, and strain level. Although all three aluminum alloys experienced void nucleation, growth, and coalescence, the extruded 6061-T6 was found to have increased necking at the higher strain rates in tension and is likely due to its initially smaller particles (precipitates) and a lower void growth rate. 5083-H131 exhibited a similar increased necking effect but to a much less extent than 6061-T6, while A356-T6 showed no evidence for strain rate difference necking. The nuances of the different strain rate and stress state effects were captured in the Horstemeyer-Gokhale [1999] void/crack nucleation model.

Based on the evidence contained in this study, the following three conclusions can justifiably be drawn:

1. The flow stress, damage, and fracture are quantifiably dependent on the applied stress state and a lesser amount on the applied strain rate.

2. The different aluminum alloys, which were processed differently, experienced void nucleation, growth, and coalescence at differing rates due to the two level void nucleation occurring at larger particles and smaller precipitates.
3. To accurately model the plasticity, damage, and fracture of these aluminum alloys, one must consider the capability of the constitutive model in capturing these stress state and strain rate differences.

REFERENCES

Agarwal, H., Gokhale, A.M., Graham, S., and Horstemeyer, M.F., "Anisotropy of Intermetallic Particle Cracking Damage Evolution in an Al-Si-Mg Base Wrought Aluminum Alloy Under Uniaxial Compression", *Metallurgical and Materials Transactions-A*, Vol. 33A, pp. 3443-3448, 2002a.

Agarwal, H., Gokhale, A.M., Graham, S., and Horstemeyer, M.F., "Quantitative Characterization of Three-Dimensional Damage Evolution in a Wrought Al-Alloy Under Tension and Compression", *Metallurgical and Materials Transactions***,** Vol. 33A, pp. 2599-2606, 2002b.

Balasundaram, A., Shan, Z., Gokhale, A.M., Graham, S., and Horstemeyer, M.F., "Particle Rotations During Plastic Deformation of 5086 (O) Aluminum Alloy", *Materials Characterization*, Vol. 48 (no. 5), pp. 363-369, 2002.

Bancroft, D., "The Velocity of Longitudinal Waves in cylindrical Bars", *Physical Review*, V59, pp. 588-593, 1941.

Bussac, M.N., Collet, P., Gary, G., and Othman, R., "An optimisation method for separating and rebuilding one-dimensional dispersive waves from multi-point measurements. Application to elastic or viscoelastic bars," *J. Mech. Phys. Solids,* V50 (2), 321-349.

Dai, S.L, Delplanque, J.-P., and Lavernia, E.J., "Microstructural Characteristics of 5083 Al Alloys Processed by Reactive Spray Deposition for Net-Shape Manufacturing," *Metallurgical and Materials Transactions A,* V29A, 2597-2611.

Dighe, M.D., Gokhale, A.M., and Horstemeyer, M. F., (1998) "Effect of Temperature on Silicon Particle Damage in Cast Microstructure of A356 Alloy," *Metallurgical and Materials Transactions*, Vol 29A, pp. 905-908.

Dighe, M.D., Gokhale, A.M., Horstemeyer, M.F., and Mosher, D.A., "Effect of Strain Rate Effect on Damage Evolution in a Cast Al-Si-Mg Base Alloy," Met. Trans A, Vol. 31A, pp. 1725-1731, 2000.

Dighe, M.D., Gokhale, A.M., and Horstemeyer, M.F., "Effect of Loading Condition and Stress State on Damage Evolution of Silicon Particles in an Al-Si-Mg base Cast Alloy", *Metallurgical and Materials Transactions-A*, Vol. 33A, PP. 555-565, 2002.

Garrison, W.M. and Moody, N.R. (1987) "Ductile Fracture," J. Physics Chem. Solids, Vol. 48, No. 11, pp. 1035-1074.

Gary, G., DAVID Manual, (2005), http://www.lms.polytechnique.fr/dynamique/greef/web4034_david.html

Gilat, A., and Wu, X., (1994) Experimental Mechanics, V 34 (2), 166-170

Goods, S.H. and Brown, L.H. (1979) "The Nucleation of Cavities by Plastic Deformation," Acta Metallurgica, Vol. 27, pp. 1-15.

Hopkinson, B., (1904), "The Effects of Momentary Stresses in Metals," Proc. Royal Soc. London, V74, 498-506.

Horstemeyer, M. F. and Gokhale, A.M., "A Void Nucleation Model for Ductile Materials," *International Journal of Solids and Structures*, Vol. 36, pp. 5029-5055, 1999.

Horstemeyer, M.F., Lathrop, J., Gokhale, A.M., and Dighe, M., "Modeling Stress State Dependent Damage Evolution in a Cast Al-Si-Mg Aluminum Alloy," *Theoretical and Applied Fracture Mechanics*, Vol. 33, pp. 31-47, 2000a.

Horstemeyer, M.F., Matalanis, M.M., Sieber, A.M., and Botos, M.L., "Micromechanical Finite Element Calculations of Temperature and Void Configuration Effects on Void Growth and Coalescence," Int J. Plasticity, Vol. 16, 2000b.

Horstemeyer, M.F. and Ramaswamy, S., "On Factors Affecting Localization and Void Growth in Ductile Metals: A Parametric Study*," Int. J. Damage Mech*., Vol. 9, pp. 6-28, 2000c.

Jones, MK., Horstemeyer, MF., Belvin, AD, "A Multiscale Analysis of Void Coalescence in Nickel," JEMT, Vol. 129, pp. 94-104, 2007.

Jordon, J.B., Horstemeyer, M.F., Solanki, K., Xue, Y., "Damage and stress state influence on the Bauschinger effect in aluminum alloys", *Mechanics of Material*, Vol. 39, pp. 920-931, 2007.

Kapoor, R., and Nemat-Nasser, S., (1998), Mechanics of Materials, (27), 1-12.

Kolsky, H., (1949), "An Investigation of the Mechanical Properties of Materials at very High Rates of Loading," Proc. Phys. Soc. B. V62 (11), 676-700.

Lindholm, U.S., Bessey, R.L. and Smith, G. V., (1971) "Effect of Strain Rate on Yield Strength, Tensile Strength, and Elongation of Three Aluminum Alloys," J. Mat., (6), 119-133.

Nicholas, T., (1981) "Tensile Testing of Materials at High Rates of Strain," Exp. Mech. V21 (5), 177-185.

Staab, G.H., and Gilat, A., (1991), Experimental Mechanics, V31, (3), 232-235

Zhao, H., and Gary, G., (1997), "A new method for the separation of waves. Application to the SHPB technique for an unlimited duration of measurement", *J. Mech. Phys. Solids,* V45 (7), 1185-1202.

CHAPTER V

COMPARING TENSION AND TORSION HOPKINSON BAR EXPERIMENTAL RESULTS FROM DIFFERENT METHODS

INTRODUCTION

Understanding material behavior and associated failure mechanics is pivotal in the development of reliable and safe yet lightweight structural components. Aluminum components have been used extensively for their high strength and stiffness to weight ratios. One theoretical key to understanding the mechanical response of materials under different stress state and strain rates is the damage evolution and fracture characteristics. Garrison and Moody (1987) gave a general review of ductile fracture for many different metal alloys with the trends being pertinent for aluminum. Essentially, ductile fracture arises from damage nucleation stemming from particle fracture or particle/matrix debonding (Goods and Brown, 1979), voids growing from these nucleation sites, and voids coalescencing after their growth has initiated (Horstemeyer et al., 2000b,c). The idea to describe material ductile failure due to nucleation, growth, and coalescences has led to the appearance of many mathematical formulations. As mentioned earlier, Horstemeyer and Gokhale (1999) developed a damage nucleation model that accounted for the stress state dependence and applied it to aluminum alloy A356 aluminum alloy. For aluminum alloys, Gokhale and co-workers have studied different nucleation damage

progression for different aluminum alloys under quasi-static loading conditions. Under quasi-static loading, Dighe et al. (1998) found that as the temperature increased, the void nucleation rate decreased for an A356 aluminum alloy. They concluded in Dighe et al. (2000) that the A356 aluminum alloy does not have a significant strain rate dependence on the damage nucleation and also quantified the stress state dependence of the damage nucleation as tests were conducted under tension, compression, and torsion for an A356 aluminum alloy (Dighe et al., 2002). One might think that since there was a clear temperature dependence on the damage nucleation, that the applied strain rate would give an inverse relationship due to dislocations and associated work hardening operating in that fashion. However, for the high rate tests, the temperature is not isothermal due to heat generation arising from plastic work. As such, clearly distinguishing the temperature and strain rate effects apart from each other is difficult under these high rate conditions. A good review of quasi-static material behavior for aluminum alloys can be found in Jordon (2007).

High strain rate testing has become increasingly more important as materials are being selected for their high strain rate response. At these strain rates (100/s to 10000/s), Hopkinson techniques are the preferred means of mechanical testing (Nemat-Nasser, 2000). The split Hopkinson pressure bar (SHPB) apparatus, first introduced by Kolsky (1949), operates by sending a pressure wave through the specimen; this pressure wave is created by launching the striker bar at the incident bar. The pressure wave passes through the incident bar and through the specimen which is held between the incident bar and the transmitter bar. Variations of the SHPB apparatus have been created for tension and torsion tests. (Al-Mousawi et al., 1997)

With regard to aluminum alloys, Dighe et al. (2002) were the first to show the experimental difference in the stress-strain response of an aluminum alloy under tension, compression, and torsion at quasi-static strain rates, and Horstemeyer et al. (2000d) modeled the associated stress-state dependence. At higher applied strain rates the stress-strain behavior under different stress-states also was significant for different aluminum alloys (up to 25% different stress levels at a particular strain level) (Tucker et al., 2009). However, in Tucker et al. (2009) the different experimental methods were not compared and contrasted in obtaining the high strain rate tension and shear data.

In this study we conclusively show the capabilities and limitations of each method by experimentally and numerically studying the mechanical response for aluminum alloy 6061-T6. In particular, specimens designed to induce tensile and torsional loading in a traditional compression Split Hopkinson Pressure Bar (SHPB) are compared with those results of direct tension and torsion specimens. Differences between stress and strain levels are investigated and explained using previous stress-state dependent data. The main contribution of this work is a comprehensive stress-state experimental and numerical analysis under dynamic loading conditions including the effect of damage under tensile loading.

HIGH STRAIN RATE TESTING TECHNIQUES

Because of the effect of the strain rate and stress-state on the plasticity and failure of a material, high strain test data in compression, tension, and torsion/shear is paramount to accurate material modeling (Tucker et al. 2009). High strain rate SHPB compression testing is a commonly used and well established method. High strain rate tension and

torsion/shear testing have been performed to a much less extent due to the inherent complexities in producing tensile or shear loading waves. Instead, there has been a focus on developing specimens with geometries that allow for tensile or torsional loading using a compressive loading pulse from a traditional SHPB. Direct tensile (Staab and Gilat 1991) and torsion (Hartley et al. 1985, Gilat Pao 1988, and Gilat and Cheng 2000) SHPB have been developed and used to successfully obtain high strain rate data. In this work, we compare results for an aluminum alloy 6061-T6 in the extruded direction from a recently developed tensile M-shaped specimen in a compression SHPB (Mohr and Gary 2007) and a commonly used shear hat specimen in a compression SHPB (Hartman 1981 and Meyer and Kruger 2000) to their direct tensile and torsion apparatus counterparts.

The M-shaped specimen (Figure 5.1) investigated here was designed by Mohr and Gary (2007) and is used to induce a plane strain tensile stress state in the gage section when tested in a compression SHPB. Mohr and Gary developed equations to extract uniaxial stress and strain assuming force equilibrium between the top and bottom faces and a uniform elastic stiffness for the specimen. Using simple equations, the force and displacement measurements at each face, and assuming plane strain in the gage section, the true and effective stress and strain can be obtained. The advantage of this design is that the specimen can be positioned freely between the incident and transmitter bars whereas conventional Hopkinson tensile techniques require the specimen to be gripped or threaded, which can alter the test results (Gray, 2000). For this M-shaped specimen, Mohr and Gary (2007) presented equations used to determine the tensile response in the gage section using the force and deformation data taken from the incident bar and transmitted bar.

Mohr and Gary (2007) employed quasi-static three-dimensional and two-dimensional dynamic finite element analyses but did not include the damage effects leading to material failure. Upon their suggestion of performing three-dimensional finite element simulations, we obliged to further validate and provide understanding of the M-shaped specimen multi-axial stress response.

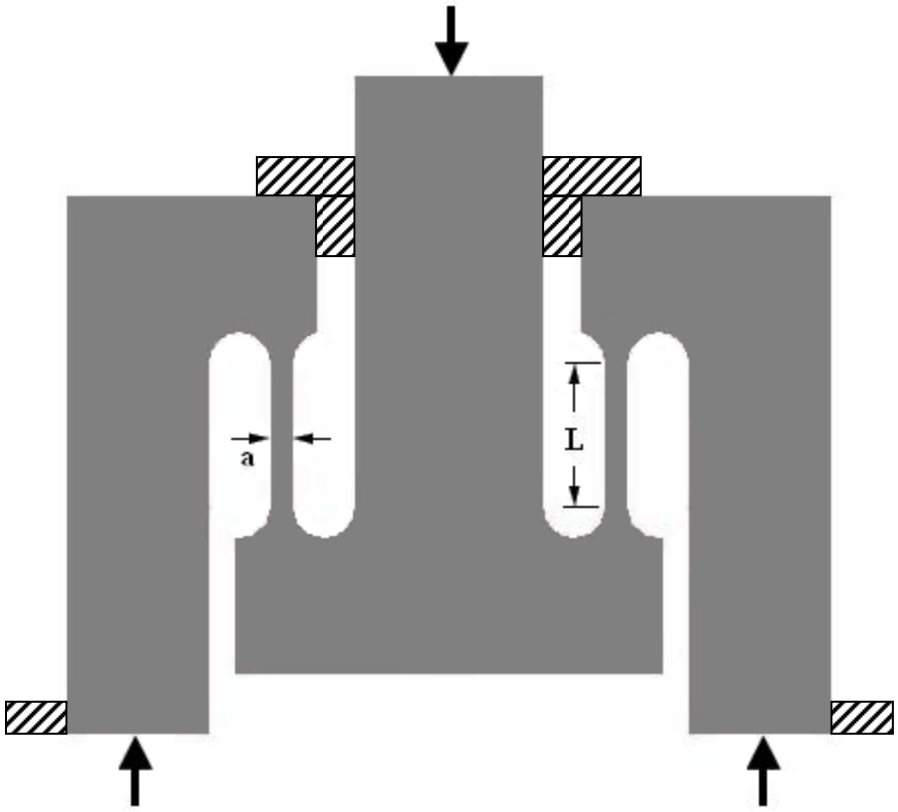

Figure 5.1. M-shaped specimen geometry presented by Mohr and Gary (2007) used to produce tensile loading in the gage section when remotely compressed. The large arrows indicate compressive loading. The hatched areas indicate the locations of the spacer blocks used to eliminate bending during testing.

In addition to the M-shaped specimen, direct tensile testing was performed. The tensile SHPB used was based on that developed by Staab and Gilat (1991). The specimen geometry was modified to a miniature dogbone shaped specimen with a gage length of 5.0 mm and gage length of 2.0 mm. The grip section was 6.5 mm wide and 3.5 mm long with a shoulder radius of 0.5 mm. The specimen was loaded via steel inserts machined to match the geometry of the grip section of the specimen and then glued to the end of the incident and transmitted bars. Three-dimensional finite element simulations were employed to verify that the effects of the notched steel section on the tensile loading wave were negligible. This specimen was proposed so that the required waiting period between tests for the adhesive used by Staab and Gilat (1990) could be avoided. In addition to the hat-shaped specimen, torsion data was obtained from a direct torsion SHPB as developed and validated by Gilat and Cheng (2000).

Hartmann et al. (1981) and Meyer and Kruger (2000) presented a hat-shaped specimen, shown in Figure 5.2, in which the gage section experiences shear dominated deformation under compressive loading. To produce this specimen, a cylinder is partially hollowed, and a groove is machined into the non-hollowed portion with only a small band retained between the two portions. This hat-shaped design is advantageous because a spacer ring may be placed in the groove to stop the experiment at a desired deformation.

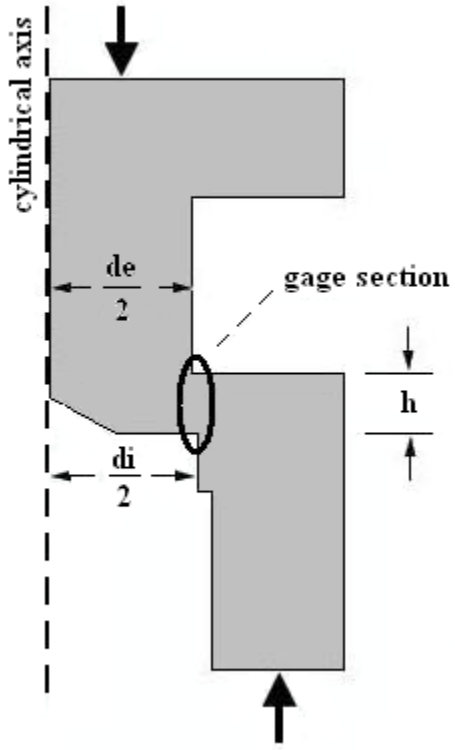

Figure 5.2. Schematic of the hat-shaped specimen presented by Meyer and Kruger (2000). This cross section is rotated about the cylindrical axis. This specimen is used to produce shear loading in the gage section when compressed. The large arrows indicate compressive loading.

EXPERIMENTAL PROCEDURES

To quantify each specimen's effectiveness in producing useful stress-strain data, the M-shaped and hat-shaped specimens were tested in a traditional compressive SHPB composed of 40 mm striker, incident, and transmitted bars of aluminum alloy 7075-T6. Loading pulses were designed to produce true strain rates of approximately 1000/s for all specimens. The strain rate is calculated using a linear curve fit of a true strain versus time plot from a strain level of 0.02 to the end of the test data for all specimens.

The direct tension tests were performed using a tension Hopkinson bar similar to that outlined by Staab and Gilat (1991). The tension bar uses a clamped section of the incident bar to induce a tensile wave that is released by breaking a pin in the clamp while the signals are measured at three locations, near the center of the incident bar past the breaker pin, near the end of the incident bar and specimen, and just past the specimen on the transmitted bars; these locations area in contrast to the two traditional locations for compression tests. The tension bars used are 12.7 mm in diameter and are made of aluminum alloy 7075-T651. The analysis method was modified by including the effect of dispersion on the tensile wave by incorporating the work of Bancroft (1941) similar to the method employed by Zhao and Gary (1997) and Bussac et al. (2002). The waves are first converted to the frequency domain using a Fast Fourier Transform and then shifted to the proper locations for analysis using the DAVID software package. This allowed for the advantages of using DAVID for analysis including the verification of force equilibrium, which is especially important for tension, because of the small level of plasticity before fracture initiation. All of the tension specimens were tested to failure.

The direct torsion tests were performed using a torsional Hopkinson bar developed after Gilat and Pao (1988). The torsion bar construction is similar to that of the tension bar in that a clamped section of the incident bar is used to induce a shear wave that is released when a breaker pin in the clamp is broken. The torsion bars used are 19.05 mm in diameter and are constructed of aluminum alloy 7075-T651. The torsion test data were analyzed in the same manner as laid out by Gilat and Wu (1994). Failure was not studied for the torsion or shear tests.

THREE - DIMENSIONAL FINITE ELEMENT ANALYSIS VALIDATION

To test the validity of the M-shaped, dogbone, and hat-shaped specimens at high rates, three-dimensional explicit finite element calculations were performed. For each specimen type, the finite element model was loaded as would be expected from the SHPB apparatus at strain rates of approximately l000/s. The incident bar is modeled as a 10.6-kg rigid plate and given an initial velocity; the transmitter bar is modeled as a 6.6-kg rigid plate and given no initial velocity. Force and displacement results were recorded at the ends of the specimens in the simulations so that the correction equations suggested by Mohr and Gary (2007) and Meyer and Kruger (2000) for the M-shaped and hat-shaped specimens respectively could be evaluated directly with experimental data. The stress and strain was also recorded in the gage section of each specimen for a comparison between the calculated stress and strain values from the correction equations. The calculations were performed using ABAQUS/Explicit (Hibbit, Karlsson & Sorensen, Inc. 2003) for the M-shaped and dogbone tensile specimens and LS-DYNA (Livermore Software Technology Corporation 2003) for the hat-shaped specimen. The material model used for each specimen, the aluminum alloy Al 6061-T6, was incorporated using the temperature-dependent and strain-rate-dependent plasticity model developed by Bammann (1990) with the damage nucleation model developed by Horstemeyer et al. (1999); the material constants were taken from Tucker et al. (2009) and are listed in Appendix A.

For the M-shaped specimen study, ABAQUS/Explicit version 6.8 was used. The simulation consisted of a quarter model of the M-shaped specimen due to the symmetry of the specimen. The M-shaped was modeled with a 0.5-mm gage width (*a* in Figure 5.1), a 2.2 mm gage length (L in Figure 5.1), and a 28.3 mm specimen depth. A refinement

study concluded that approximately 34,000 elements yielded a converged solution to the given problem. A constant velocity of 3 m/s was applied to the top of the specimen normal to the surface to yield an approximate strain rate of 1000^{-s} in the gauge section. The bottom of the specimen was held fixed in the direction normal to the face. This simulates a rigid wall condition which is an adequate approximation for this study. The spacers needed to restrict bending in the specimen were applied by fixing displacement of the parts of specimen affected by the spacers. The simulation was allowed to run until damage reached its maximum value of 0.99 in a single element which indicates failure.

The second simulation consists of a tension bar experiment where a dogbone specimen is held by cylindrical grips. The tensile dogbone specimen was modeled with a 2.0 mm gage width, a 5.0 mm gage length, and 0.5 mm shoulder radii. The steel inserts were modeled as deformable bodies to include the effect of the elastic deformation of the inserts during loading. A refinement study concluded approximately 9000 elements yielded the converged solution. This allowed for 3 elements through the half thickness of the dogbone specimen. One end of the grips was loaded with a constant pressure of 8.2 MPa, while the displacement in the loading direction on the other end of the grips was held fixed. This pressure was determined by experimental data from the analogous tension bar experiment. The tangential contact interaction between the specimen and the grips was modeled using a friction coefficient of 0.1. The friction coefficient was varied between 0.1 and 0.5 with no appreciable difference evident. The simulation was allowed to run until a single element achieved a damage value of 0.99 as with the M-shaped simulation.

The hat-shaped specimen was modeled with a 5.0 mm internal diameter (d_i in Figure 5.2), a 4.8-mm external diameter (d_e in Figure 5.2), a 1.0 mm gage height, a 0.1 mm gage width, a 10.0 mm total diameter, and a 10.0 mm total height. Because this specimen is symmetrical around the cylindrical axis, only a small piece needed to be modeled; for easy boundary condition application, a quarter specimen was modeled. Simulations were completed using an initial incident plate velocity of 300 mm/s, which produced a 1000/s recorded shear strain rate.

RESULTS

In this section, we first describe the compression results, followed by the torsion/shear experiments, and then followed by both types of tension results. Figure 5.3 shows the stress-strain behavior of the aluminum alloy 6061-T6 under compression at a strain rate of 1000/s. The response is typical of aluminum under high strain rate compression with a relatively linear hardening regime following yielding.

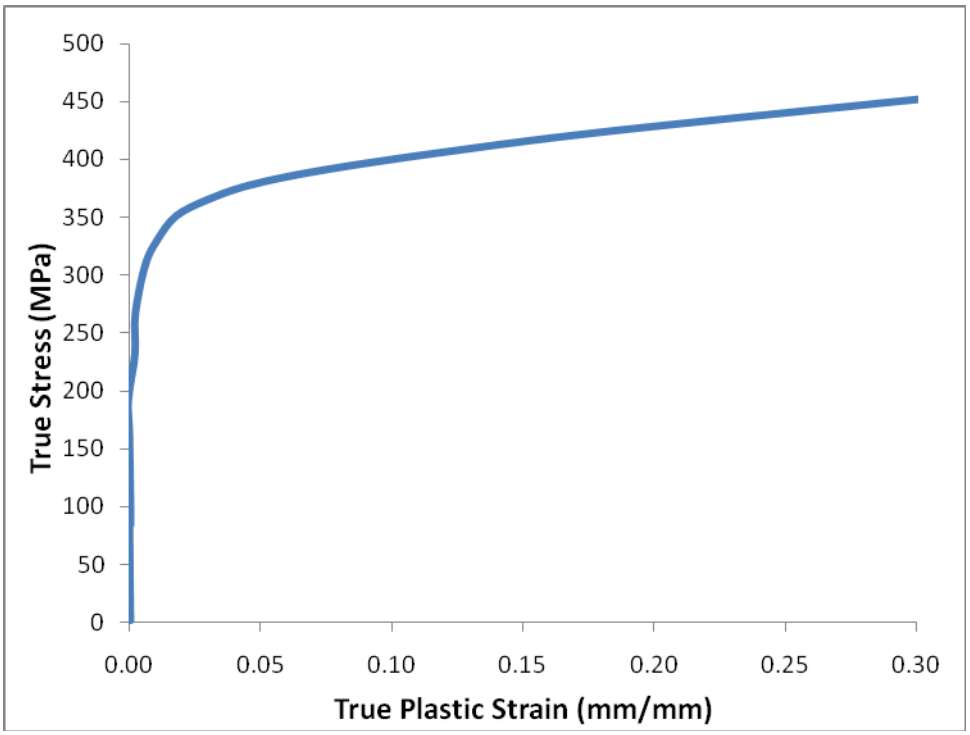

Figure 5.3. Compression SHPB stress-strain behavior of aluminum alloy 6061-T6 at a strain rate of 1000/s.

To quantify the torsion/shear behavior of the aluminum alloy 6061-T6, the shear stress and uniaxial stress are shown in Figure 5.4 for the hat-shaped specimen (shear under SHPB compression). In order to compare the torsion and shear results, an assumption relating torsion and simple shear is warranted. In particular, if one assumes that the curvature related to the torsional circumferential normal strain is negligible, then the stress response in simple shear and torsion is identical from a continuum perspective. In the case of the hat-shaped shear specimen, the shear stress reached a level of 241.2 MPa at 6% plastic strain. The gage section showed a dominant shear stress state as expected with some minor compression stresses characteristic of fixed-end simple shear. However, larger uniaxial stresses arose but were was largely confined to the non-gage section of the specimen.

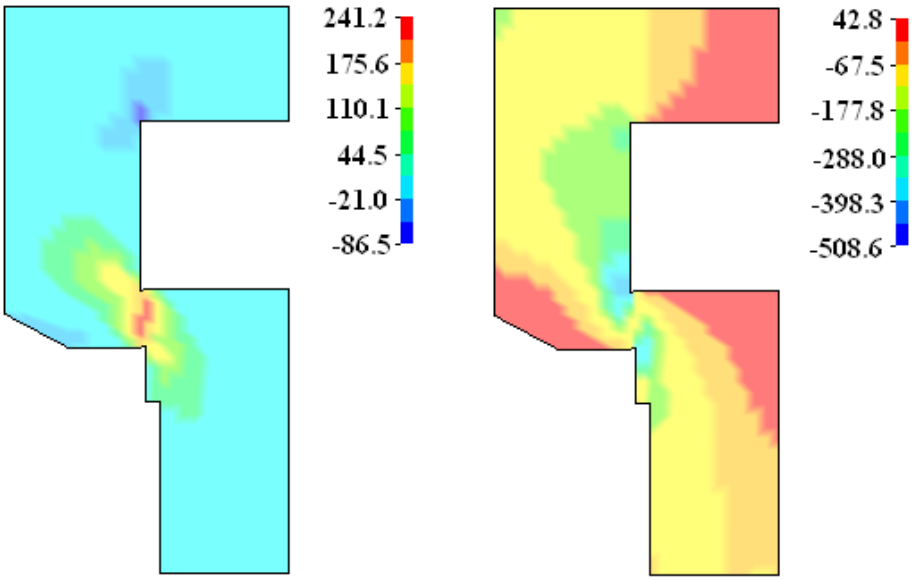

Figure 5.4. Stress contour plots of the hat-shaped specimen (shear under SHPB compression) showing the (a) shear stress and (b) uniaxial stress at a plastic shear strain level of 6%. Stress units are in MPa.

To investigate the specimen's results, the recorded shear stress and strain in the gage section were compared with the calculations proposed by Meyer and Kruger (2000) using the force and displacements of the specimen ends. The results of the hat-shaped specimen showed that the recorded shear stresses agreed well because all of the compressive forces were balanced in the shear zone. However, the shear strains did not agree; this discrepancy occurred because the compression of the non-gage sections was not considered. To correct for this, the stiffness of the non-gage sections was then used to account for the non-gage deformation. The non-gage stiffness of the specimen was determined by a static finite element calculation, in which the gage section was removed and replaced by rigid boundary conditions. A 700-N applied load resulted in a 0.0223-

mm compression; so the stiffness of the specimen's non-gage portions was 31.45 kN/mm for the quarter model, or 125.79 kN/mm for the whole specimen. For this geometry and a 0.33 Poisson's ratio, the stiffness of the non-gage sections is the modulus of elasticity times 1.8214 mm. The following shear strain equation was derived, assuming only simple shear deformation in the gage section:

$$\gamma = \frac{\Delta H - \frac{F}{K}}{w} \tag{5.1}$$

where ΔH is the specimen's height change, F is the compressive force, and w is the gage width. Figure 5.5 shows a comparison of the torsion/shear data obtained from the direct torsion experiment and shear-hat specimen experiment and simulation. The shear-hat experiment and simulation use Equation 1 to correct the shear strain.

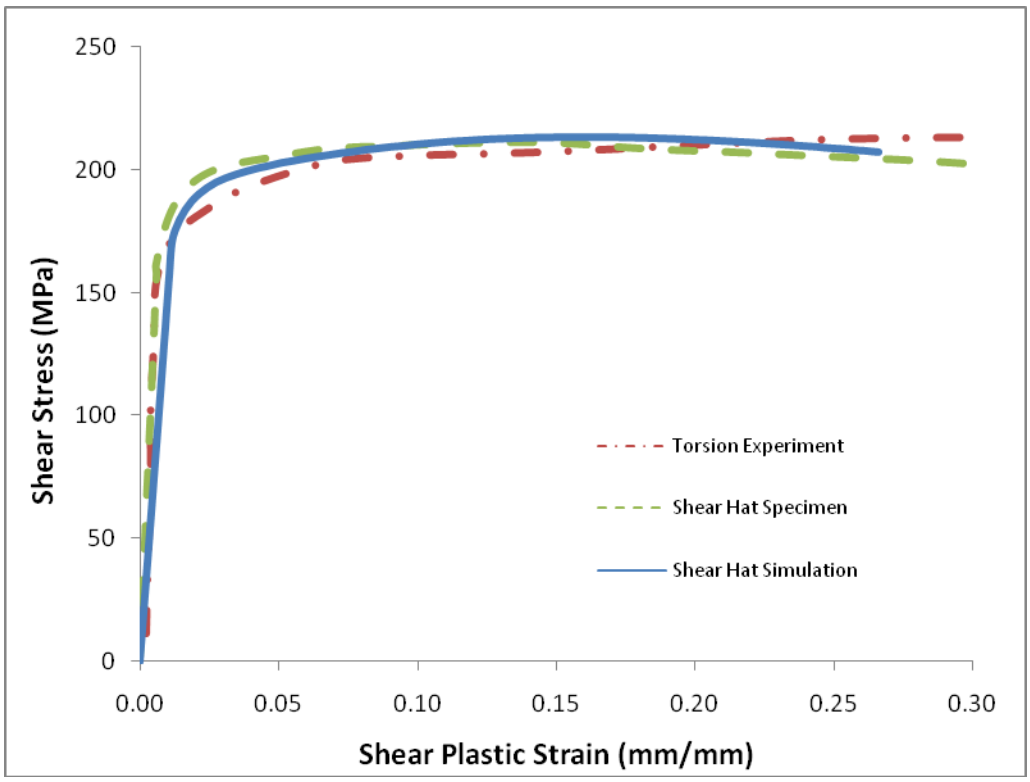

Figure 5.5. Shear stress-strain results of aluminum alloy 6061-T6 for the direct torsion experiment and hat-shaped specimen experiment and simulation showing good agreement between both shear stress and strain after correcting for the compression in the non-gage section.

For tension two different methods were employed as described earlier. The dogbone tensile specimen tested under the direct tension SHPB was found to be under nearly uniform uniaxial tension during the entirety of the test. Figure 5.6 shows the stress triaxiality in the specimen at 3% effective plastic strain and at the onset of localization.

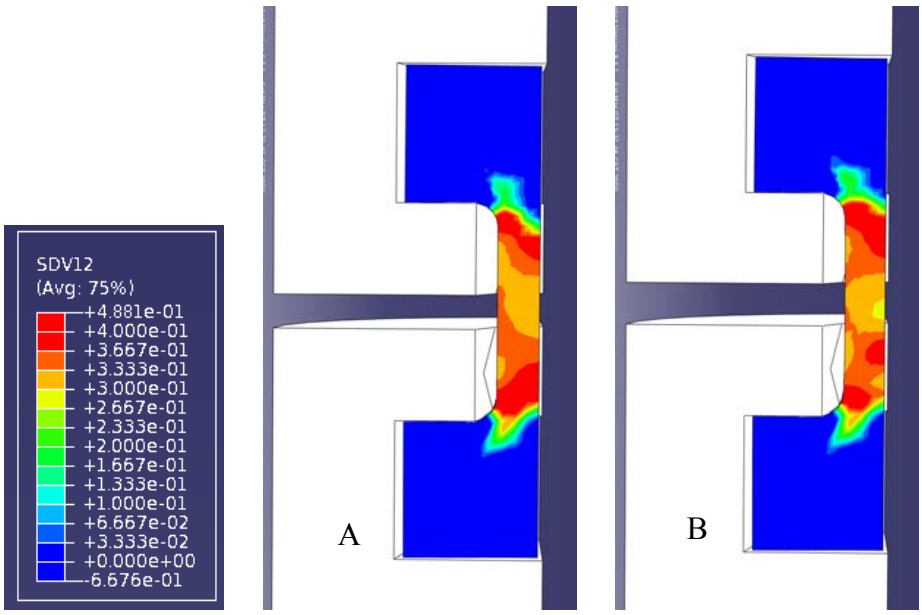

Figure 5.6. Stress triaxiality (SDV12) in the gage section of the direct tension SHPB dogbone specimen (a) at 3% effective plastic strain and (b) at the onset of localization showing nearly a uniform uniaxial tensile stress state (triaxiality = 0.33).

The stress distribution found in the M-shaped specimen (tension under SHPB compression) was influenced by the bending forces. From bending effects, the uniaxial stress was greatest in the top-left and bottom-right corners of the gage section when viewed from the front of the specimen as shown in Figure 5.1. As the specimen experienced higher levels of deformation, this bending was subsumed by a greater uniaxial tensile force. As deformation further increased, a fairly uniform stress field representing plane tensile strain conditions was achieved soon after yielding as shown below in Figure 5.7, which shows the stress triaxiality, defined as the hydrostatic stress divided by the von Mises stress, at 3% effective plastic strain and at localization, respectively. The triaxiality in the major part of the section with also a more uniform stress state was approximately 0.66. A narrow section on the front face with a width of

less than 6 mm was under uniaxial tension, reinforcing the findings of Mohr and Gary (2007).

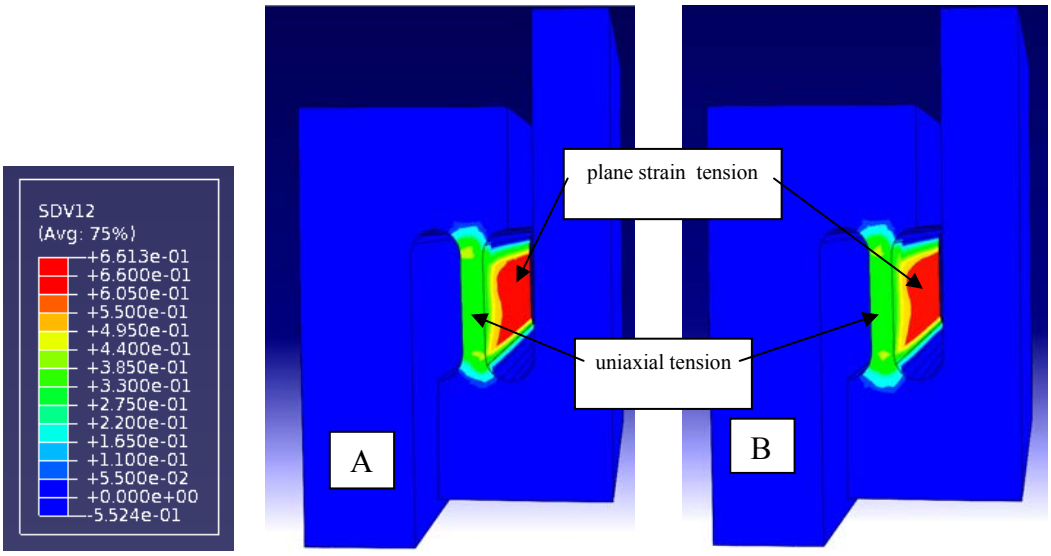

Figure 5.7. Stress triaxiality (SDV12) in the gage section of the M-shaped specimen (a) at 3% effective plastic strain and (b) at the onset of damage localization showing nearly uniform tensile plane strain stress state.

To investigate the M-shaped specimen results, the recorded uniaxial stress and strain in the gage section were compared with calculations by Mohr and Gary (2007) (Equations 2-7) used to account for the compressive deformation in the gage section and the results from the uniaxial dogbone specimen. For these calculations, the specimen stiffness, K, was determined by a static finite element calculation, where a 0.015-mm compressive displacement was applied. The calculated reaction force and subsequent stiffness were 642 N and 42.8 kN/mm, respectively. Since this value is material dependent, these constants must be determined for each material being tested. Stress and

plastic strain were recorded in the middle of the gage section on the back symmetrical plane of the quarter model which corresponds to the midway point of the gage section of the full specimen. The force and displacement of the specimen ends were recorded and used in the following calculations proposed by Mohr and Gary (2007).

$$\Sigma_{.yy}(t) = \frac{F(t)}{A_{.o}} \tag{5.2}$$

where Σ_{yy} is the nominal stress along the gage section, F is the force measured at the transmitted bar-specimen interface, and A_o is the total initial cross sectional area of the gage section of the specimen.

$$E_{yyp}(t) = \frac{u(t)}{l_{eff}} - \frac{F(t)}{K \cdot l_{eff}} \tag{5.3}$$

where E_{yyp} is the nominal plastic strain, u is the difference in the displacement measured at the incident bar-specimen interface and transmitted bar-specimen interface, l_{eff} is the gage length, and K is the stiffness of the specimen previously described.

$$\sigma_{yy} = \left(1 + E_{yyp}\right) \cdot \Sigma_{yy} \tag{5.4}$$

where σ_{yy} is the true uniaxial stress.

$$\varepsilon_{yyp} = \ln\left(1 + E_{yyp}\right) \tag{5.5}$$

where ε_{yyp} is the true plastic strain.

The equivalent plastic strain and von Mises stress, assuming transverse plane strain conditions become:

$$\varepsilon_{eff}(t) = \frac{2}{\sqrt{3}} \cdot \varepsilon_{yyp}(t) \tag{5.6}$$

$$\sigma_{eff}(t) = \frac{\sqrt{3}}{2} \cdot \sigma_{yy}(t) \tag{5.7}$$

Comparing the data obtained from experimental results with the M-shaped specimens and applying the associated calculations described above allows for a direct comparison to uniaxial tensile data obtained using the direct tension dogbone specimen. The associated stress values were lower than those recorded in the specimen, arising from the more complex stress state in the gage section during the initial plastic loading of the M-shaped specimen. The M-shaped specimen also showed a lower elongation to failure than the dogbone specimen due to a higher stress triaxiality value which increases the damage rate. This elongation to failure difference was verified using measurements taken in a scanning electron microscope. Figure 5.8 shows the true stress-strain and effective stress-effective strain results of the dogbone direct tensile specimen and the M-shaped plane strain tensile specimen with the simulation results of each.

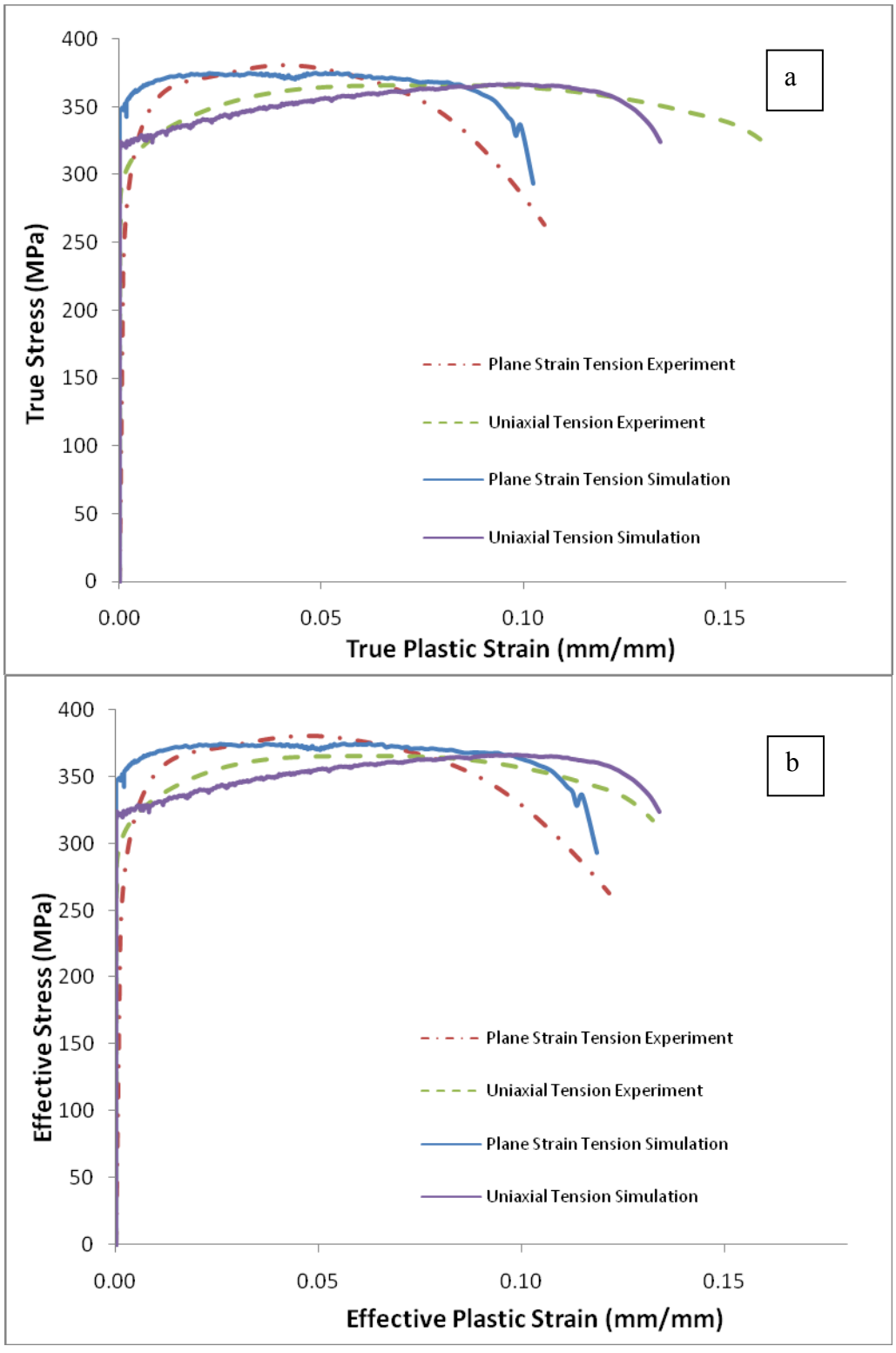

Figure 5.8. Stress-strain comparison for aluminum alloy 6061-T6 from dogbone direct tension specimen and M-shaped plane strain tension specimen test data and simulations with true stress-strain on the left (a) and effective stress-strain on

the right (b). The initial uniaxial stress in the M-shaped specimen was higher than the direct dogbone specimen due to a more complex stress state in the initial stages of loading. The difference in the elongation to failure is due to the triaxiality differences in the gage sections of the specimens.

DISCUSSION

Each of the proposed specimens can give valuable insight to the behavior of a material under varying stress states. The complexities of the testing methods and resulting stress states must be taken into account when analyzing or comparing data however. This is especially true if accurate modeling of the failure and fracture of a material is desired. The shear hat specimen was found to give very accurate results compared to a direct torsion specimen for both shear stress and strain to a plastic shear strain of approximately 30% once a correction factor was employed.

The M-shaped specimen was found to slightly over-estimate stress due to a complex stress state during initial plasticity. The onset of failure was also found to be underestimated due to higher stress triaxiality in the gage section of the specimen which leads to a higher damage evolution rate. To further investigate the effect of the stress state on the fracture of the M-shaped and dogbone specimens, the true strain tensors were compared at four strain levels: the onset of plasticity, 3% effective plastic strain, the onset of localization, and failure. The results were used to construct a forming limit diagram after the work of Horstemeyer (2000a). The forming limit diagram reinforced the earlier simulation results in that the dogbone specimen was found to be under nearly uniaxial tensile stress and a majority of the M-shaped specimen was under plane strain tensile conditions with the front face experiencing nearly uniaxial tension. Figure 5.9 shows the

forming limit diagram constructed with the test data. In the diagram, the major strain is plotted against the minor strain and the values where localization and failure occur in various loading scenarios are plotted. In this case, the strain tensors at two locations in the dogbone specimen: near the shoulder and the middle of the gage section, and three locations on the M-shaped specimen: the middle of the front face, the middle of the rear symmetric face, and the midpoint between the two, were used. Since the simulation ended when one element reached a damage level of 0.99, only that element location was used to calculate the localization and failure strain levels. These locations were the middle of the dogbone specimen and the midpoint of the gage section of the M-shaped specimen.

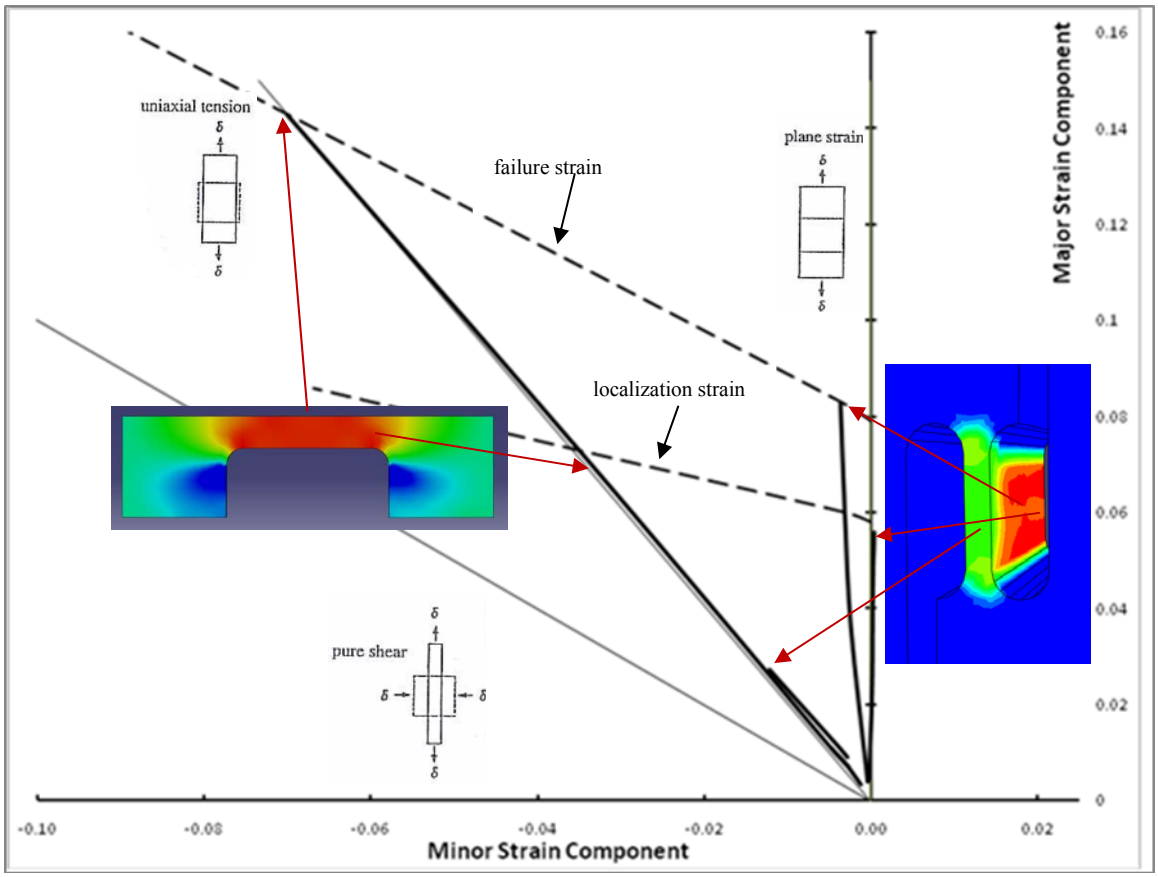

Figure 5.9. Forming limit diagram of aluminum alloy 6061-T6 showing various strain states and the results of the simulations of the M-shaped plane strain and dogbone uniaxial tension test. The y-axis represents major strain component and the x-axis represents the minor strain component. The thin lines represent common deformation modes in strain space and the thicker lines represent the data collected from the finite element analysis at the locations indicated. The dashed lines indicate limits for localization and failure as calculated from the finite element analysis. Only the locations at which failure occurred was used to calculate the failure and localization strain levels. The major strain of the dogbone specimen at failure is higher than that of the M-shaped specimen as the testing results exhibited. The arrow endpoints represent the maximum strain level attained during the simulation.

The results of all five experiments performed in this study are shown in Figure 5.10. Significant effects from the stress state on the plasticity and failure of the material are evident.

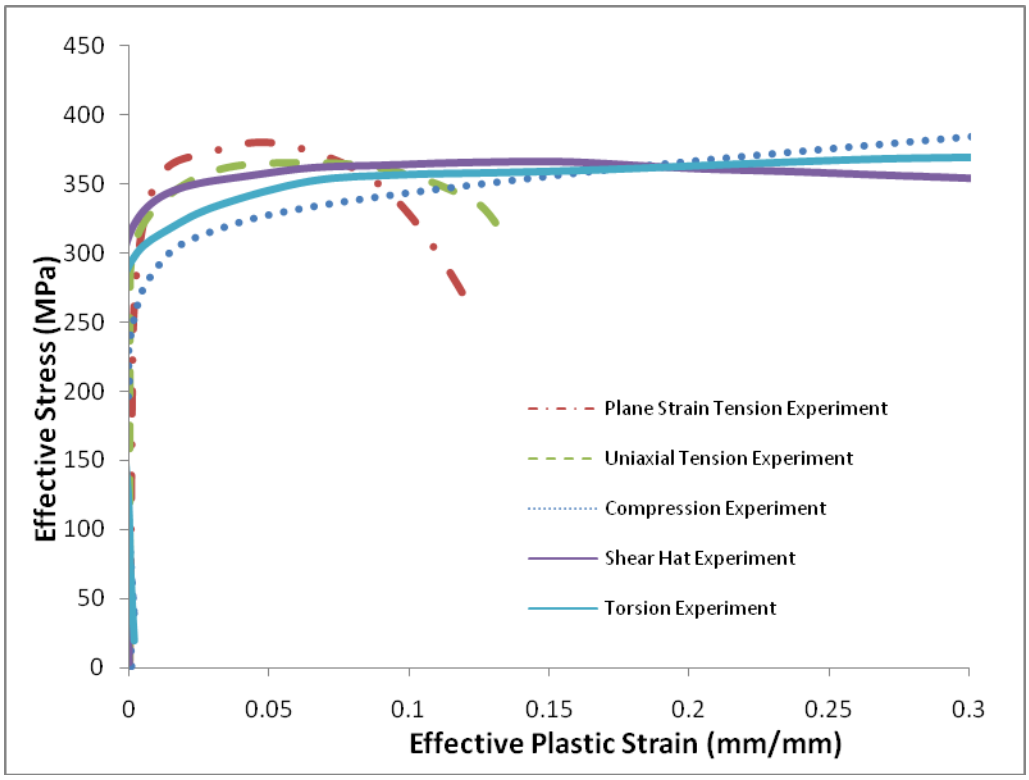

Figure 5.10. Results of each of the experimental methods investigated in this work showing significant stress state effects on the plasticity and failure of aluminum alloy 6061-T6 at true strain rates of ~1000/s and ambient temperature.

The results from a high strain rate compression test (Tucker et al. 2009), the M-shaped plane strain tension test, and the hat-shaped shear test using the same SHPB setup are shown in Figure 5.11. The M-shaped and hat-shaped specimen results were calculated

based on the work by Mohr and Gary (2007) and Meyer and Kruger (2000) respectively. The data shows that the stress state has a significant effect on the plasticity, damage, and failure of the material. A material model capable of capturing the stress state and strain rate dependence of a material is critical for accurately predicting the effects of dynamic events.

Both the hat-shaped shear specimen and the M-shaped plane strain tension specimen performed well in predicting flow stress and plasticity to the point of localization. Since damage is dependent not only on stress state, but also the microstructural features of a material, the behavior of a material under plane strain conditions is not sufficient for predicting damage localization and failure. Any correction factors beyond that recommended by Mohr and Gary (2007) would be valid only for the specific material being tested. The data obtained from plane strain tension tests can certainly provide valuable insight to the behavior of a material by isolating the effect of the stress state in its damage and failure characteristics given that uniaxial tensile data is previously available. A new tensile specimen design was presented as a way to alleviate some of the problems inherent in gripping specimens and was found to produce a nearly uniaxial stress state in the gage section from the onset of yielding to damage localization. The complexities related to generating a tensile loading pulse and determining the behavior of the stress wave at the specimen-bar interface are still present however, making the testing procedure and data analysis more complicated than a traditional SHPB compression test.

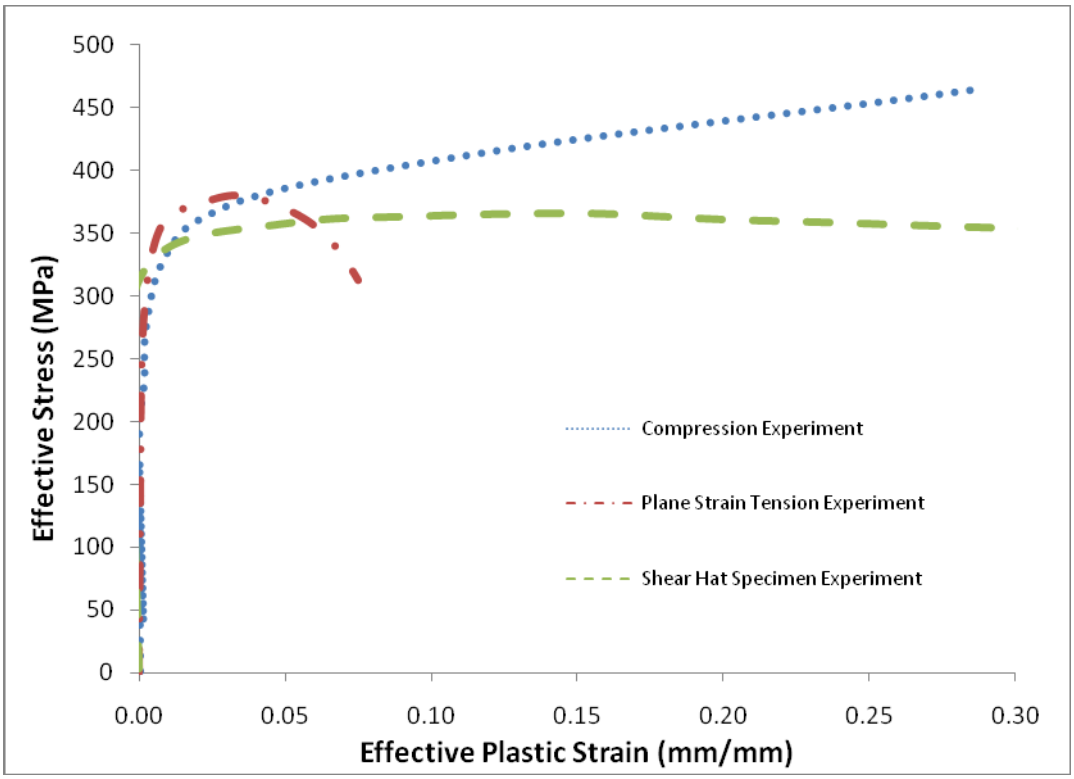

Figure 5.11. Comparison of test data obtained from three tests in the same SHPB apparatus of different geometries designed to induce compressive, plane strain tensile, and shear stress states at true strain rates

CONCLUSIONS

Based on the results of this study, it was determined that the hat-shaped shear specimen was an adequate substitute for a direct torsion test using the equations provided by Meyer and Kruger (2000) since the gage section undergoes nearly uniform shear stress to a plastic shear strain level of approximately 30%. The dogbone specimen was found to produce a uniaxial tensile stress state in the gage section to the point of damage localization. The M-shaped specimen was found to produce a transverse plane strain stress state in a majority of the gage section to the onset of localization.

The transverse plane strain condition present in the M-shaped specimen provides an excellent method for model validation and a deeper understanding of the effect of the stress state on the damage evolution and failure characteristics. Accurate uniaxial tensile data is still necessary to truly capture the effects of the stress state, strain rate, and microstructural features on the plasticity, damage, and failure on a material. If, however, a simpler modeling technique not so concerned with damage and failure is adequate, the hat-shaped shear and M-shaped plane strain specimens can provide reliable results using a traditional SHPB in compression. The ultimate decision must be based on the level of fidelity required for a given project.

REFERENCES

Al-Mousawi, M.M., Reid, S.R., and Deans, W.F. "The Use of the Split Hopkinson Pressure Bar Techniques in High Strain Rate Materials Testing," *Proceedings of the Institution of Mechanical Engineers*, vol. 211, C, 273-292, 1997.

Bammann, D.J., "Modeling the Temperature and Strain Rate Dependent Large Deformation of Metals," *Applied Mechanics Review*, vol. 43, 5, part 2, S312-S319, 1990.

Bancroft, D., "The Velocity of Longitudinal Waves in cylindrical Bars", *Physical Review*, V59, pp. 588-593, 1941.

Bussac, M.N., Collet, P., Gary, G., and Othman, R., "An optimisation method for separating and rebuilding one-dimensional dispersive waves from multi-point measurements. Application to elastic or viscoelastic bars," *J. Mech. Phys. Solids,* V50 (2), 321-349.

Dighe, M.D., Gokhale, A.M., and Horstemeyer, M. F., (1998) "Effect of Temperature on Silicon Particle Damage in Cast Microstructure of A356 Alloy," *Metallurgical and Materials Transactions*, Vol 29A, pp. 905-908.

Dighe, M.D., Gokhale, A.M., Horstemeyer, M.F., and Mosher, D.A., "Effect of Strain Rate Effect on Damage Evolution in a Cast Al-Si-Mg Base Alloy," *Met. Trans A*, Vol. 31A, pp. 1725-1731, 2000.

Dighe, M.D., Gokhale, A.M., and Horstemeyer, M.F., "Effect of Loading Condition and Stress State on Damage Evolution of Silicon Particles in an Al-Si-Mg base Cast Alloy", *Metallurgical and Materials Transactions-A*, Vol. 33A, PP. 555-565, 2002.

Garrison, W.M. and Moody, N.R. (1987) "Ductile Fracture," J. Physics Chem. Solids, Vol. 48, No. 11, pp. 1035-1074.

Gary, G., DAVID Manual, (2005), http://www.lms.polytechnique.fr/dynamique/greef/web4034_david.html

Gilat, A., Cheng, C.S.. "Torsional split Hopkinson bar tests at strain rates above 10^4 s^{-1}," *ExperimentalMechanics,* V40, 54–59. 2000.

Gilat, A., and Pao, Y.H., "High-rate decremental-strain-rate test," *Experimental Mechanics,* V28 (3), 322-325. 1988

Goods, S.H. and Brown, L.H. (1979) "The Nucleation of Cavities by Plastic Deformation," Acta Metallurgica, Vol. 27, pp. 1-15.

Gray III, G.T., "Classic Split-Hopkinson Pressure Bar Testing," *ASM Handbook* (edited by Kuhn, H. and Medlin, D.), V 8, 462-476, ASM International, 2000.

Guo, Y.B., Wen, Q., and Horstemeyer, M.F., "An Internal State Variable Plasticity-Based Approach to Determine Dynamic Loading History Effects on Material Property in Manufacturing Processes," *International Journal of Mechanical Sciences*, vol. 47, 1423-1441, 2005.

Hartley, K.A., Duffy, J., Hawley, R.W., "The torsional Kolsky (split Hopkinson) bar," ASM Metal Handbook, V. 8, 9th Edition. American Society ofMetals, Materials Park, OH, pp. 218–228. 1985.

Hartmann, K.-H., Kunze, H.D., and Meyer, L.W., "Metallurgical Effects on Impact Loaded Materials," *Shock Wave and High-Strain-Rate Phenomena in Metals* (edited by Meyers, M. A. and Murr, L. E.), 325-337, Plenum Press, 1981.

Hibbit, Karlsson & Sorensen, Inc., "ABAQUS/Explicit User's Manual, ver. 6.3," Pawtucket, 2002

Horstemeyer, M. F. and Gokhale, A.M., "A Void Nucleation Model for Ductile Materials," *International Journal of Solids and Structures*, Vol. 36, pp. 5029-5055, 1999.

Horstemeyer, M.F., Lathrop, J., Gokhale, A.M., and Dighe, M., "Modeling Stress State Dependent Damage Evolution in a Cast Al-Si-Mg Aluminum Alloy," *Theoretical and Applied Fracture Mechanics*, Vol. 33, pp. 31-47, 2000d.

Horstemeyer, M.F., "A Numerical Parametric Investigation of Localization and Forming Limits," International Journal of Damage Mechanics, Vol. 9, No. 3, 255-285, 2000a.

Horstemeyer, M.F., Matalanis, M.M., Sieber, A.M., and Botos, M.L., "Micromechanical Finite Element Calculations of Temperature and Void Configuration Effects on Void Growth and Coalescence," Int J. Plasticity, Vol. 16, 2000b.

Horstemeyer, M.F. and Ramaswamy, S., "On Factors Affecting Localization and Void Growth in Ductile Metals: A Parametric Study*," Int. J. Damage Mech*., Vol. 9, pp. 6-28, 2000c.

Jordon, J.B., Horstemeyer, M.F., Solanki, K., Xue, Y., "Damage and stress state influence on the Bauschinger effect in aluminum alloys", *Mechanics of Material*, Vol. 39, pp. 920-931, 2007.

Kolsky, H., "An Investigation of the Mechanical Properties of Materials at Very High Rates of Loading," *Proceedings of the Physical Society*, vol. 62, B, 676-700, 1949.

Livermore Software Technology Corporation, *LS-DYNA Keyword User's Manual*, Livermore, California, 2003.

Meyer, L.W. and Kruger, L., "Shear Testing with Hat-Shaped Specimen," *ASM Handbook* (edited by Kuhn, H. and Medlin, D.), vol. 8, 451-452, ASM International, 2000.

Mohr, D. and Gary, G., "M-shaped Specimen for the High-Strain Rate Tensile Testing Using a Split Hopkinson Pressure Bar Apparatus," *Experimental Mechanics*, accepted for publication, 2007.

Nemat-Nasser, S., "Introduction to High Strain Rate Testing," *ASM Handbook* (edited by Kuhn, H. and Medlin, D.), vol. 8, 427-461, ASM International, 2000.

Staab, G.H., and Gilat, A., "A direct-tension split Hopkinson bar for high strain-rate testing," *Experimental Mechanics,* V31 (3), 232-235, 1991.

Tucker, M.T., Horstemeyer, M.F., Whittington, W.R., Solanki, K.N., and Gullett, P.M., "The Effect of Varying Strain Rates and Stress States on the Plasticity, Damage, and Fracture of Aluminum Alloys," *Mechanics of Materials,* submitted

Zhao, H., and Gary, G., (1997), "A new method for the separation of waves. Application to the SHPB technique for an unlimited duration of measurement", *J. Mech. Phys. Solids,* V45 (7), 1185-1202.

CHAPTER VI

SUMMARY AND FUTURE WORK

SUMMARY

A methodology in which the microstructure-property relationships of a material pertaining to stress state and strain rate dependence has been developed. A variety of materials formed using different methods were included in the study to determine its robustness. An internal state variable model was implemented to capture the effects of the various microstructural features and loading histories and was validated by predicting and explaining the onset of damage localization and failure in a transverse plane strain tension specimen under high strain rate loading. The study showed the importance of high fidelity experimentation and modeling techniques necessary to accurately predict the response of a component to complex dynamic loading.

A wrought magnesium alloy was tested under compression at varying strain rates and loading orientations. The effect of the deformation mechanisms active in each orientation was explained and pertinent microstructural properties were documented. Three different aluminum alloys were tested under varying strain rates in tension, torsion, and compression and the resulting effects on the microstrutural evolution were quantified and implemented into the internal state variable damage model. The effect of particle sizes on the failure mechanism was studied and conclusions were drawn and validated via

microscopic and image analysis methods. The resulting material modeling constants were then used to compare the results of techniques for acquiring tension and torsion/shear high strain rate data. The limitations of the methods were discussed and the importance of accurate experimental and modeling methods were again highlighted. A mixture of experimental and modeling results were used to reveal the damage mechanisms responsible for the plasticity, damage, and failure under varying loading scenarios.

FUTURE WORK

Significant experimental and modeling progress must be made in the understanding of the anisotropic effects on textured magnesium alloys especially. The complexities involved in modeling the loading orientation dependencies on active deformation mechanisms is a significant hurdle to overcome and will require carefully planned experimental work designed to accurately follow the evolution of twinning as a function of strain rate, stress state, and temperature. A model must also be developed that is capable of capturing the microstructural history changes related to twinning as well. A study of the stress state dependence of AZ31 similar to that performed on the aluminum alloys in Chapter IV would offer significant insight into the role of the deformation mechanisms under varying conditions. Furthermore, the effect of the adiabatic heating on the mechanical response of AZ31 should be studied in more detail to shed light on the thermodynamics involved in twinning dominated deformation.

The work presented here shows that a systematic approach of various stress-strain testing coupled with microstructural observations of the materials investigated are

capable of providing the information needed to accurately predict the behavior of components subjected to complex loading conditions. The method should be expanded to determine its viability for a wider variety of materials including polymers and biological specimens. There is still much room for improvement in the standardization of these techniques though and more novel materials will inevitably complicate the task. A detailed investigation into the uncertainty of each of the testing methods is certainly warranted. Standard designs for high strain rate specimens could significantly help in improving repeatability of tests. A standard method for quantifying pertinent microstructural features would also help to remove the inherent subjectivity currently present.

APPENDIX

ISV MODEL CONSTANTS FOR 6061-T6 ALUMINUM ALLOY IN THE EXTRUDED DIRECTION

Table A.1. Microstructure-property (elastic-plastic) model constants for 6061-T6 aluminum alloy tested in the extruded direction.

6061-T6	Constants	Value
Constants for J/B formulas for G and K	G (MPa)	25900
	a	0
	Bulk (MPa)	67500
	b	0
	melt temp (K)	855.13
Specifies the yield stress	C1 (MPa)	3.157
	C2 (K)	0
	C3 (MPa)	276
	C4 (K)	0
	C5 (1/MPa)	0.005
	C6 (K)	0
Kinematic hardening and recovery terms	C7 (1/MPa)	0.693
	C8 (K)	0
	C9 (MPa)	739.5
	C10 (K)	0
	C11 (sec/MPa)	0
	C12 (K)	0
Isotropic hardening and recovery terms	C13 (1/MPa)	0.95
	C14 (K)	0
	C15 (MPa)	539.3
	C16 (K)	12
	C17 (sec/MPa)	0
	C18 (K)	0
Hardening & recovery cons.	Ca	567.441
	Cb	-0.21
Temperature	init.temp (K)	298
	heat gen. Coeff.	0.372024

Table A.2. Microstructure-property (damage) model constants for 6061-T6 aluminum alloy tested in the extruded direction.

	Constants	Value
McClintock Void Growth (primary)	void growth exp	0.3
	init. Rad. (mm)	0.001
Nucleation (primary)	a	892
	b	235
	c	63
	nuc coeff	7.25
	fract. Toughness MPa($m^{1/2}$)	29
	part. Size (mm)	0.0013
	part. Vol fract.	0.0085
Coalescence	cd1	0.1
	cd2	0
	cd3	0
	dcs0 (mm)	30
	dcs (mm)	300
	dcs exp. Zz	0
CA pore growth	init. Void vol. Fract.	0.00001
Nucleation	nuc. Temp. depend.	0
Coalescence	coal. Temp. depend	0
Yield strength Adjustment terms	c19	0.0119
	c20	-9.9